University of Zurich UZH

Advancing the quantification of CO2 and NOx emissions from power plants using Sentinel-5P observations: A novel approach to address NOx chemistry in plumes

ESS 511 Master's Thesis

Author
Sandro Meier
18-706-481

Supervised by
PD Dr. Gerrit Kuhlmann (gerrit.kuhlmann@empa.ch)

Faculty representative
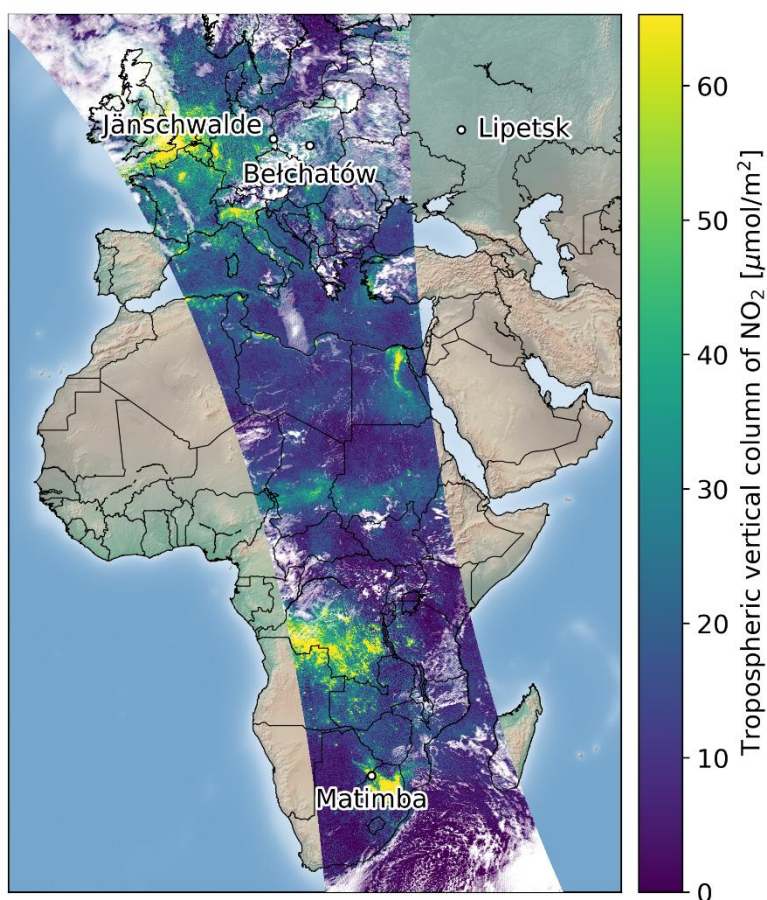Prof. Dr. Alexander Damm

09.08.2023
Department of Geography, University of Zurich

UNIVERSITY OF ZURICH

Master Thesis

Advancing the quantification of CO_2 and NO_x emissions from power plants using Sentinel-5P observations:
A novel approach to address NO_x chemistry in plumes

MSc in Earth System Science
Sandro Meier
18-706-481

Supervisor: PD Dr. Gerrit Kuhlmann, Empa
Faculty Member: Prof. Dr. Alexander Damm, RSL

Submission of Thesis: 9th August 2023

Abstract

As climate change progresses, 195 countries have committed to reducing their CO_2 emissions under the Paris Agreement. To ensure the credibility of these reductions, independent verification using satellites is essential. Satellite observations facilitate the estimation of CO_2 emissions from large point sources, such as power plants. Since measuring CO_2 directly is challenging, nitrogen oxides ($NO + NO_2 = NO_x$), which are co-emitted during combustion, can be used as a proxy for determining CO_2 emissions. However, satellites can only measure NO_2, necessitating a conversion into NO_x. Previous studies have used a constant conversion factor of 1.32 which greatly simplified the NO_x chemistry. Therefore, the aim of this work is to develop a more realistic model for a conversion factor of NO_2 to NO_x and apply it to data from the TROPOMI instrument on the Sentinel-5P satellite for the years 2020 and 2021.

More realistic conversion factors are derived using the cross-sectional flux method. To achieve this, the NO and NO_2 fields in existing high-resolution chemistry transport simulations of three power plants and a metallurgical plant are analysed. From these, NO_2-to-NO_x conversion factors are derived which depend on the time since emission. In addition, two methods for calculating representative wind speeds for the cross-sectional flux method are implemented and the influence of TROPOMI air mass factors on tropospheric NO_2 columns in plumes is evaluated.

The results indicate that the NO_2 columns in the analysed plumes require an air mass factor correction by a factor of 1.1 to 1.4. With this correction, the estimated annual NO_x emissions with their uncertainties are within the range of the bottom-up reported emissions. The biases are reduced from between -50 and -60% to only between -12 and -23%. Single-overpass estimates can be quantified with an uncertainty of 20-27%, while annual NO_x emission estimates have uncertainties in the range of 3-16% and are highly dependent on the number of successful retrievals.

The approach for converting NO_2 into NO_x discussed in this study is limited by the generalisation of the derived NO_2-to-NO_x conversion factors for different meteorological and trace gas background conditions. In addition, the study highlights the need for further research on the calculation of a representative wind speed and air mass factors. This study thus marks a decisive step towards a global, uniform, high-resolution, and near real-time estimation of CO_2 emissions – especially with regard to upcoming NO_2 monitoring satellites such as Sentinel-4 and -5.

Keywords: CO_2, NO_x, emission quantification, cross-sectional flux method, ddeq, MicroHH, NO_x:NO_2 ratios, Sentinel-5P, TROPOMI, air mass factor

Acknowledgements

Content

List of Figures

List of Tables

List of Abbreviations

AMF	**A**ir **M**ass **F**actor
BG	**B**ackground
CAMS	**C**opernicus **A**tmosphere **M**onitoring **S**ervice
CO2M	**CO$_2$ M**onitoring
CO2MVS	**CO$_2$ M**onitoring and **V**erification **S**upport Capacity
CoCO2	**Co**pernicus **CoCO$_2$** project
ddeq	**D**ata **D**riven **E**mission **Q**uantification
DOAS	**D**ifferential **O**ptical **A**bsorption **S**pectroscopy
ECMWF	**E**uropean **C**entre for **M**edium-Range **W**eather **F**orecasts
ENTSO-E	**E**uropean **N**etwork of **T**ransmission **S**ystem **O**perators for **E**lectricity
E-PRTR	**E**uropean **P**ollutant **R**elease and **T**ransfer **R**egister
ERA5	**E**CMWF **Rea**nalysis v**5**
ESA	**E**uropean **S**pace **A**gency
EUMETSAT	**Eu**ropean Organisation for the Exploration of **Met**eorological **Sat**ellites
GEMS	**G**eostationary **E**nvironment **M**onitoring **S**pectrometer
GNFR	**G**ridded **N**omenclature **f**or **R**eporting
IFS	**I**ntegrated **F**orecasting **S**ystem
MicroHH	A high-resolution numerical fluid dynamics model
NO$_x$	Nitrogen oxides, consisting of nitric oxide and nitrogen dioxide
O$_3$	Ozone
OCO	**O**rbiting **C**arbon **O**bservatory
PBL	**P**lanetary **B**oundary **L**ayer
RF	**R**andom **F**orest regression
SCD	**S**lant **C**olumn **D**ensity
Sentinel-5P	**Sentinel-5** Precursor
SNR	**S**ignal-to-**N**oise **R**atio
SZA	**S**olar **Z**enith **A**ngle
TEMPO	**T**ropospheric **E**missions: **M**onitoring of **Po**llution
TM5-MP	**T**racer **M**odel Version **5** – **M**assively **P**arallel Version
TROPOMI	**Tropo**spheric **M**onitoring **I**nstrument
VCD	**V**ertical **C**olumn **D**ensity
VOC	**V**olatile **O**rganic Compound

1 Introduction

Under the Paris Agreement, 195 Parties have committed to limiting global warming to well below 2°C compared to pre-industrial temperatures (UNFCCC, 2015; United Nations, 2015). This requires drastic reductions of anthropogenic greenhouse gas emissions such as CO_2. In order to monitor emission reductions, the Parties of the Paris Agreement must regularly report their emissions based on national inventories (referred to as a bottom-up approach). However, to date, no global observation system exists that allows for independent monitoring of anthropogenic emissions and verification of bottom-up reported emissions (Pinty et al., 2017). Such a system is also needed because it can reduce uncertainties and fill gaps in national emission inventories. The plan is to assimilate the estimated emissions into the reanalysis dataset of the Integrated Forecasting System (IFS) by the European Centre for Medium-range Weather Forecasts (ECMWF) (Agustí-Panareda et al., 2023). Therefore, emission data should be available in near real time. A convenient method to obtain such high-resolution, uniform global emission estimates is to use satellite observations (Koene et al., 2021; Pinty et al., 2017).

For this reason, the Copernicus CO_2 Monitoring (CO2M) mission has been initiated by the European Commission, the European Space Agency (ESA), the European Organisation for the Exploration of Meteorological Satellites (EUMETSAT) and ECMWF (Pinty et al., 2020). The mission will consist of up to three satellites measuring, among others, column-averaged dry air mole fractions of CO_2 and tropospheric NO_2 columns and will be launched in 2025 (EoPortal, 2021; ESA Earth and Mission Science Division, 2020). One aim is to quantify CO_2 emissions from point sources such as industrial complexes, large cities, and power plants, because they account for the majority of anthropogenic CO_2 emissions (Kuhlmann et al., 2021). For example, power generation alone was responsible for more than 40% of global fossil CO_2 emissions in 2021 (Crippa et al., 2022).

Several case studies have investigated the potential and limitations of quantifying point source CO_2 emissions from space (Bovensmann et al., 2010; Goldberg et al., 2019a; Kuhlmann et al., 2021, 2018; Liu et al., 2020; Nassar et al., 2017; Reuter et al., 2019). In parallel, a range of methods has been developed to estimate CO_2 emissions. One of them is the cross-sectional flux method which is implemented in a Python package called "data driven emission quantification" (*ddeq*) (Kuhlmann et al., 2021, 2020, 2019). With this method, emissions are determined by dividing a plume into several cross-sections. For each cross-section, the column densities are integrated, resulting in line densities, which are converted into fluxes using the wind speed.

Under the assumption of steady-state conditions, the emissions can be estimated from the fluxes of each polygon along the plume (Kuhlmann et al., 2021).

However, there remain several challenges when trying to estimate CO_2 emissions from satellites. Among them are a high sensitivity to cloud cover, large natural sinks and sources, and a low signal-to-noise ratio (Koene et al., 2021).

To circumvent these problems, several studies have proposed using nitrogen oxides (NO_x = NO + NO_2), which are co-emitted with CO_2 during high-temperature combustion processes, to quantify CO_2 emissions (Goldberg et al., 2019a; Kuhlmann et al., 2021, 2018; Liu et al., 2020; Reuter et al., 2019). The NO_x estimates can then be converted to CO_2 emissions using bottom-up reported CO_2:NO_x emission ratios (Goldberg et al., 2019a; Kuhlmann et al., 2021; Liu et al., 2020). On top of that, there are a number of existing and upcoming satellites that provide NO_2 products with high accuracy, making the use of NO_x to quantify CO_2 emissions very appealing. One of these is the TROPOspheric Monitoring Instrument (TROPOMI) on the Sentinel-5 Precursor satellite which has a much better temporal and spatial coverage than the upcoming CO2M mission due to its larger swath (Veefkind et al., 2012). It provides daily observations of NO_2 and other trace gases with a spatial resolution of 3.5 x 5.5 km^2 (van Geffen et al., 2022; Veefkind et al., 2012). Several case studies have shown that TROPOMI data can be used to estimate NO_x emissions from cities and power plants (Douros et al., 2023; Goldberg et al., 2019b; Lorente et al., 2019).

However, estimating CO_2 emissions from NO_x observations also comes with its drawbacks. One is the fact that satellites only measure NO_2 but not NO_x. NO_2 must therefore be converted to NO_x, taking into account the complex chemistry of NO_x. Nonetheless, previous studies have only implemented a highly simplified representation of NO_x chemistry, using a constant factor of 1.32 to convert NO_2 to NO_x (e.g., Beirle et al., 2011; Kuhlmann et al., 2021).

Therefore, the aim of this study is to develop a more realistic model for a conversion factor of NO_2 to NO_x that accounts for the spatiotemporal variations of NO_x chemistry in plumes. This is done using the examples of the power plants Bełchatów (PL), Jänschwalde (DE), Matimba and Medupi (ZA) (hereafter referred to as Matimba), as well as a metallurgical plant in Lipetsk (RU). The advances are implemented into the existing cross-sectional flux algorithms of the *ddeq* package.

The analysis is conducted in the following seven steps:

1. Analysis of the CO_2, NO, and NO_2 fields in existing high-resolution chemistry transport simulations to identify how the NO_x:NO_2 concentration ratio and the NO_x lifetime varies along the plume, over time and for the different cases.

2. Evaluation of the spatiotemporal evolution of wind fields to convert the length of a plume into time since emission.

3. Development of a model to describe the NO_2-to-NO_x conversion factor as a function of the time since emission that takes NO_x chemistry within plumes into account.

4. Validation of the new NO_2-to-NO_x conversion factor with high-resolution chemistry transport simulations where the true emissions are known.

5. Application of the improved method to TROPOMI NO_2 observations for the four point sources over a two year period. This requires the correction of biases in the air mass factors (AMFs) of the TROPOMI data (e.g., Douros et al., 2023).

6. Assessment of the time series of TROPOMI estimates using bottom-up reported emissions available from annual emission reports which are interpolated to higher temporal resolution using power generation data.

7. Analysis of the temporal variability of NO_x emissions in the TROPOMI time series and the resulting uncertainty of the annual emission estimates.

The working hypothesis is that these implementations allow more accurate estimates of NO_x and consequently CO_2 emissions from NO_2 observations, which are required for global monitoring of CO_2 emissions in the context of the Paris Agreement.

2 Theoretical Background

2.1 The Copernicus CO_2 project

The Copernicus CO_2 project (CoCO2) is a project within the Horizon 2020 programme and includes 25 partners from European countries. It was launched in 2021 with the aim of building the prototype for a European Monitoring and Verification Support capacity of CO_2 emissions (CO2MVS) in support of the Paris Agreement. Such a system consists of a numerical model assimilating CO_2 emission data from observations, regional inversions, and emission inventories (CoCO2, 2023).

As part of the CoCO2 project, several numerical transport models were implemented and evaluated to determine the models' ability to realistically simulate the fundamental characteristics of plumes. The models were run for the three coal-fired power plants Bełchatów (PL), Jänschwalde (DE), and Matimba (ZA), the metallurgical plant Novolipetsk in Lipetsk (RU), and the three megacities Berlin (DE), Paris (FR), and Randstad (NL). Among the models, some simulated tropospheric chemistry (LOTUS-EUROS, MicroHH, WRF CHEM) while others did not (COSMO-GHG, ICON-ART). This library of plumes was used to compare the model simulations run with different settings such as resolution and numerical schemes, with satellite observations of NO_2 as well as in-situ aircraft measurements of CO_2 (Koene and Brunner, 2023).

2.2 Measuring CO_2 from space

One of the inputs to the CO2MVS for the assimilation of CO_2 emissions will be satellite observations. They offer the advantage of estimating CO_2 emissions globally at a high spatiotemporal resolution and in near real time (Koene et al., 2021; Pinty et al., 2017). However, estimating CO_2 emissions using satellites has several issues. First, the observations have a high sensitivity to clouds permitting only observations with a cloud cover of less than 1% to be used (Koene et al., 2021; Kuhlmann et al., 2021). It is therefore expected that a constellation of three CO2M satellites will be able to retrieve estimates of CO_2 emissions on a maximum of 50 days per year (ESA Earth and Mission Science Division, 2020). However, anthropogenic CO_2 emissions fluctuate on daily, weekly, and seasonal time scales. As a result, the temporal resolution of CO_2 estimates has a strong influence on the uncertainties in quantification (Kuhlmann et al., 2021). Second, CO_2 has high background concentrations and large natural sinks and sources such as photosynthesis and respiration. These produce CO_2 signals of similar magnitude to the enhancements due to anthropogenic sources. Plumes can thus be altered, leading to erroneous emission

estimates (Koene et al., 2021; Kuhlmann et al., 2021). Third, CO_2 measurements have a low signal-to-noise ratio (SNR) due to the higher background concentrations which makes the detection CO_2 plumes less reliable (Koene et al., 2021; Kuhlmann et al., 2019; Reuter et al., 2019). Finally, there is currently no satellite capable of imaging CO_2 concentrations of plumes, and CO2M will not be launched until 2025 (EoPortal, 2021; ESA Earth and Mission Science Division, 2020).

2.3 Measuring NO_x from space

One way to avoid these challenges is to estimate CO_2 via the emissions of nitrogen oxides (NO_x = NO + NO_2), which are co-emitted with CO_2 during high-temperature combustion processes (Seinfeld and Pandis, 2006). Satellites such as Sentinel-5 Precursor (Sentinel-5P) (see section 2.5) and the Geostationary Environment Monitoring Spectrometer (GEMS) already offer NO_2 observations at high temporal resolution. They will be complemented by the launch of further satellites such as the geostationary Tropospheric Emissions: Monitoring of Pollution (TEMPO) and Sentinel-4 as well as the polar-orbiting Sentinel-5 (EoPortal, 2023, 2014, 2013). Using NO_x to estimate CO_2 emissions has the advantage that NO_x has lower background concentrations, leading to a higher SNR and a higher contrast of anthropogenic plumes. Besides, the short lifetime of NO_x leads to sharper plumes compared to CO_2 (Goldberg et al., 2019a; Koene et al., 2021). As a result, the detection of NO_x plumes is more reliable (Kuhlmann et al., 2021; Reuter et al., 2019). Furthermore, there are negligible natural NO_x sources which could influence anthropogenic plumes. On top of that, NO_x is less sensitive to cloud cover whereby observations with 30% cloud fraction can still be used (Beirle et al., 2021; Goldberg et al., 2019a; Koene et al., 2021; Kuhlmann et al., 2021). Consequently, using observations of NO_x to quantify CO_2 emissions doubles the number of successful retrievals per year (Kuhlmann et al., 2021).

Despite these advantages, estimating CO_2 emissions from NO_x observations also comes with its challenges. The first source of uncertainty is the fact that estimated NO_x emissions must be converted to CO_2 emissions using the ratio of bottom-up reported emissions of CO_2 and NO_x (Berezin et al., 2013; Goldberg et al., 2019a; Kuhlmann et al., 2021). These must be source-specific because the amount of NO_x emissions depends on fuel type, combustion temperatures, the operating conditions of the furnace, and post-combustion removal of NO_x (Pronobis, 2020). However, bottom-up emission inventories are not reported for all point sources and are often estimated based on proxies such as fuel consumption rather than the continuous monitoring of flue gas concentrations (IPCC, 2006). Despite, applying bottom-up reported CO_2:NO_x emission

ratios currently is the most appealing approach because the uncertainties of other methods such as CO_2:NO_x ratios estimated directly from satellite observations are much higher (Kuhlmann et al., 2021). A second source of uncertainty in estimating CO_2 emissions from NO_x observations is the fact that satellites can only measure NO_2 but not NO_x. This is due to the short lifetime, low concentrations, and the weak absorption signal of NO (Pietrzyk et al., 2010). Consequently, in order to determine NO_x concentrations from measured NO_2 concentrations, NO_2 must be converted taking into account the NO_x chemistry. As satellite images of NO_2 are taken around noon, the daytime tropospheric chemistry is most relevant.

2.4 Daytime tropospheric NO_x chemistry

Unlike CO_2, NO_x undergoes a series of chemical and photochemical reactions in the troposphere: While more than 90% of NO_x from combustion processes is emitted as NO (Pronobis, 2020), it is rapidly oxidised to NO_2 in the presence of ozone (O_3) with a lifetime of seconds to minutes (Kimbrough et al., 2017; Seinfeld and Pandis, 2006):

$$NO + O_3 \longrightarrow NO_2 + O_2 \tag{2.1}$$
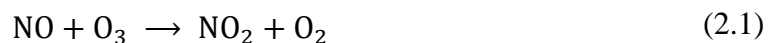
The rate of this reaction depends on several factors such as the concentration of O_3 and volatile organic compounds (VOCs), as well as solar radiation and temperature (Kimbrough et al., 2017; Seinfeld and Pandis, 2006). Subsequently, NO_2 is mainly removed by reacting with OH radicals with lifetimes ranging from hours to a few days in the lower troposphere (Jaffe, 2003; Seinfeld and Pandis, 2006):

$$NO_2 + OH \stackrel{+M}{\longrightarrow} HNO_3 \tag{2.2}$$

Where M denotes a collision partner. Again, the exact NO_2 lifetime is influenced by many factors such as temperature, the amount of NO_2, OH radicals, which in turn depends on O_3, humidity, VOC levels and solar radiation (Jaffe, 2003; Seinfeld and Pandis, 2006).

As NO cannot be measured by satellites, it has to be included in the conversion of NO_2 to NO_x. However, previous studies which have quantified NO_x from satellite observations have applied a highly simplified conversion. For example, they used a constant NO_x:NO_2 ratio of 1.32 to convert NO_2 measurements to NO_x (e.g., Beirle et al., 2011; Kuhlmann et al., 2021). This assumption was derived from the photo-stationary state for typical urban conditions, assuming NO_x and O_3 concentrations of 100 ppb each (Seinfeld and Pandis, 2006):

$$\frac{[NO_x]}{[NO_2]} = 1 + \frac{j_{NO_2}}{k_1 \cdot [O_3]} \tag{2.3}$$

Where j_{NO_2} denotes the photolysis rate of NO_2 and k_1 is the reaction coefficient of the oxidation of NO with O_3 in Eq. (2.1). However, NO_x concentrations in the plume of point sources are orders of magnitude higher than 100 ppb (Skalska et al., 2010). Thus, O_3 is rapidly titrated within the plume, resulting in NO_x:NO_2 ratios which exceed 1.32. It can be produced again through the HO_x/NO_x cycle: a series of reactions initiated by the oxidation of VOCs originating from biogenic or anthropogenic hydrocarbon emissions. In chemical reactions, they are denoted by RH where R represents any alkyl group (Seinfeld and Pandis, 2006):

$$RH + OH \xrightarrow{+O_2} RO_2 + H_2O \tag{2.4}$$

However, this reaction is suppressed by the reaction in Eq. (2.2), which consumes the OH radicals due to its higher rate coefficient for an average urban mix of VOCs. Only when the VOC:NO_2 ratio exceeds 5.5:1 does O_3 start to form again (Seinfeld and Pandis, 2006). This occurs at the edges of the plume where surrounding air masses containing VOCs are mixed in as well as further along the plume when the NO_2 concentration decreases with increasing ageing of the plume through removal by the reaction in Eq. (2.2). Therefore, increasingly more NO is oxidised the older the plume is and the NO_x:NO_2 ratio approaches the value of 1.32. The HO_x/NO_x cycle includes photolysis reactions which occur at a higher rate when more energetic radiation is available (Seinfeld and Pandis, 2006).

On the bottom line, the assumption of a constant NO_x-to-NO_2 conversion factor of 1.32 has led to significant underestimations of NO_x and hence CO_2 emissions (e.g., Beirle et al., 2021; Hakkarainen et al., 2023; Liu et al., 2020). In some studies, this underestimation went unnoticed because the bottom-up reported emissions did not include all sources, e.g., the Medupi power plant in Hakkarainen et al. (2021) and Potts et al. (2023).

2.5   Sentinel-5P

In October 2017, the Copernicus Sentinel-5P satellite was launched by ESA, the European Commission and the Netherlands Space Office. It was the first satellite of the Sentinel series devoted to observing the Earth's atmosphere (ESA, 2022; Veefkind et al., 2012). Since then, the satellite has been orbiting the Earth in a near-polar sun-synchronous orbit with an overpass time at 13:30 local time.

The only payload on board of Sentinel-5P is the TROPOspheric Monitoring Instrument (TRO-POMI) which is a spectrometer that allows it to monitor a wide range of atmospheric constituents important for air quality, such as carbon monoxide (CO), formaldehyde (CH_2O), methane (CH_4), nitrogen dioxide (NO_2), ozone (O_3) and sulphur dioxide (SO_2), as well as aerosols and clouds (Veefkind et al., 2012).

With its push-broom scanner, TROPOMI covers a 2'600 km wide swath, providing daily global coverage. This is an important feature because trace gas concentrations in the troposphere vary on small time scales. Compared to its predecessors, TROPOMI has an unprecedented high signal-to-noise ratio of 1'500 for NO_2 (van Geffen et al., 2022) and a high spatial resolution of initially 3.5 km along and 7 km across-track (Veefkind et al., 2012) which has been improved to 3.5×5.5 km^2 since August 2019 (van Geffen et al., 2019).

For the retrieval of NO_2 concentrations, the TROPOMI data is processed using a differential optical absorption spectroscopy (DOAS) which derives the total quantity of NO_2 along the optical path from the sun to the satellite (Platt and Stutz, 2008; van Geffen et al., 2019). These slant column densities (SCDs) contain both the stratospheric and tropospheric NO_2. In a second step, the SCDs are assimilated into the 3D chemistry-transport model TM5-MP, which simulates a range of atmospheric reactive trace gases with a spatial resolution of $1° \times 1°$ and a temporal resolution of 30 minutes (Williams et al., 2017). The rationale behind this approach is to assimilate the retrieved SCDs into the model, aiming to achieve optimal concordance between the TM5-MP and TROPOMI SCDs in regions with negligible tropospheric NO_2 content (e.g., over remote oceans). Consequently, the total SCDs in these areas are effectively equivalent to the stratospheric SCDs. As these show little variation in space, the retrieved stratospheric SCDs can be subtracted from the total columns to obtain the tropospheric contribution (Williams et al., 2017). In a third step, the SCDs are converted to vertical column densities (VCDs) using an air mass factor (AMF) (van Geffen et al., 2019):

$$VCD = \frac{SCD}{AMF} \tag{2.5}$$

The AMF depends on the vertical profile of NO_2 from TM5-MP and is calculated as follows (van Geffen et al., 2019):

$$AMF = \frac{\sum_l m_l \cdot c_l \cdot x_l}{\sum_l x_l} \tag{2.6}$$

Here, m_l denotes the AMF in layer l, c_l a temperature correction term and x_l the a-priori NO_2 concentration in layer l. The altitude dependent AMFs m_l are calculated using a radiative

transfer model based on, among other parameters, the surface albedo, cloud properties, as well as the satellite viewing geometry (van Geffen et al., 2019). In the TROPOMI data product, they are given as a ratio to the total AMF and are referred to as averaging kernels. They are an indication of the measurement sensitivity of NO_2 in each layer. An averaging kernel of 1 means that the satellite instrument has perfect sensitivity to the trace gas at that altitude. Dark surfaces decrease the averaging kernels, while bright surfaces and optically thick clouds increase the averaging kernels above the cloud top. Below the cloud top they are close to 0 (Eskes and Boersma, 2003).

Due to its coarse resolution, the TM5-MP model cannot resolve plumes from power plants or cities. As a result, the modelled NO_2 profiles x_l are lower than the true concentrations within plumes in the lower atmosphere, where the averaging kernels are the smallest. This leads to an overestimation of the AMF according to Eq. (2.6) and therefore to an underestimation of the NO_2 VCDs according to Eq. (2.5). Such a bias over polluted regions has also been shown in previous studies (Griffin et al., 2019; Verhoelst et al., 2021). Therefore, the estimated NO_x emissions were underestimated by up to a factor of two (Beirle et al., 2021, 2019; Goldberg et al., 2019b). As a consequence, a correction for the bias in the AMFs must be implemented (see section 4.7).

2.6 Estimating emissions with the cross-sectional flux method

As satellites observe the atmosphere from above, they measure atmospheric constituents as vertically integrated columns. These must be converted into fluxes to determine the emissions from point sources. To this end, several methods have been developed and applied in recent years. The four most promising approaches were reviewed in a study by Varon et al. (2018) to quantify point sources of methane from satellite observations. Of these, they considered the cross-sectional flux method to be one of the most promising: It is least prone to errors due to turbulence, has a comparatively simple physical basis and can deal with missing values in the plume.

In the cross-sectional flux method, emissions are determined by dividing a plume into several cross-sections perpendicular to the plume. For each cross section, the mass of the trace gas enhancement over the background $\Delta\Omega$ is integrated over the width of the plume which yields line densities. These are multiplied by the wind speed U to obtain the trace gas flux Q (Koene et al., 2021; Varon et al., 2018):

$$Q = \int_{-\infty}^{+\infty} U(x,y) \cdot \Delta\Omega(x,y)dy \qquad (2.7)$$

Here, x denotes the along plume direction while y denotes the across plume direction.

The challenge lies in the requirement of the wind speed U to be represented as a 2D field. However, plumes are transported by 3D winds which vary greatly with height. Therefore, the 3D wind field must be vertically averaged to represent the effective wind speed within the plume (see section 4.2). For most applications, the representation of the 2D wind field has been simplified under the assumption of a constant wind speed U_{eff} throughout the plume. Subsequently, Eq. (2.7) is simplified to

$$Q = U_{\mathrm{eff}} \cdot \int_{-\infty}^{+\infty} \Delta\Omega(x,y)dy \qquad (2.8)$$

where the trace gas flux Q becomes equivalent to the emissions.

The cross-sectional flux method does not work when the wind deviates from steady-state conditions and when the wind speed is too low (< 2 m/s). In this case, the wind directions are more variable (Varon et al., 2018). Furthermore, it is not possible to resolve overlapping plumes when sources are clustered (Koene et al., 2021).

2.7 Data-driven emission quantification

The data-driven emission quantification (*ddeq*) package in Python is a collection of algorithms for estimating trace gas emissions from hot spots such as cities and power plants (Kuhlmann et al., 2021, 2020, 2019). It was originally developed around the cross-sectional flux method but now includes several other approaches such as the Gaussian plume inversion method, integrated mass enhancement and more (Kuhlmann et al., 2023). The details of the cross-sectional flux method as well as the propagation of uncertainty are described in Kuhlmann et al. (2021). It is implemented for the quantification of NO_x emissions as follows and illustrated in Figure 2.1 using a TROPOMI image as an example:

The first step is to detect plumes that have significantly enhanced NO_2 VCDs above the background. This is done by applying a z-test to the SNR of NO_2. The detected pixels are grouped into coherent plumes and assigned to a source which is taken from a list of point sources (black crosses in Figure 2.1a). In a second step, the local background VCD is calculated by applying a low-pass filter to the pixels around the detected plume under the assumption of a spatially

smooth background. The estimated background is then subtracted from the VCDs of the detected plume to isolate the point source emission signals of NO_2. In a third step, a second order polynomial is fitted to the plume to represent the centre line (black line in Figure 2.1a). Based on this, all pixels are transformed into a plume coordinate system with the dimensions along and across the plume. The plume is then divided into several polygons with fixed spacing whereby the length of a polygon depends on the resolution of the satellite image (yellow polygons in Figure 2.1a). Within each polygon, the line densities of NO_2 are calculated by fitting a Gaussian curve to the VCDs of the pixels inside the polygon (Figure 2.1b). This approach employs the information of all plume pixels for the quantification and is more robust to missing values than taking line cross-sections. The NO_2 line densities are converted to fluxes using the effective wind speed at which the plume was transported. Under the assumption of constant wind speeds (see section 2.6), a weighted vertical mean of the horizontal wind speed at the source is used. The NO_2 fluxes are converted to NO_x by multiplication with a constant factor of 1.32. In a final step, a negative exponential function is fitted to the fluxes along the plume to account for NO_x chemistry (see section 2.4) (Figure 2.1c). The intercept of this function represents the estimated emissions while the inverse of the decay parameter corresponds to the estimated NO_x lifetime.
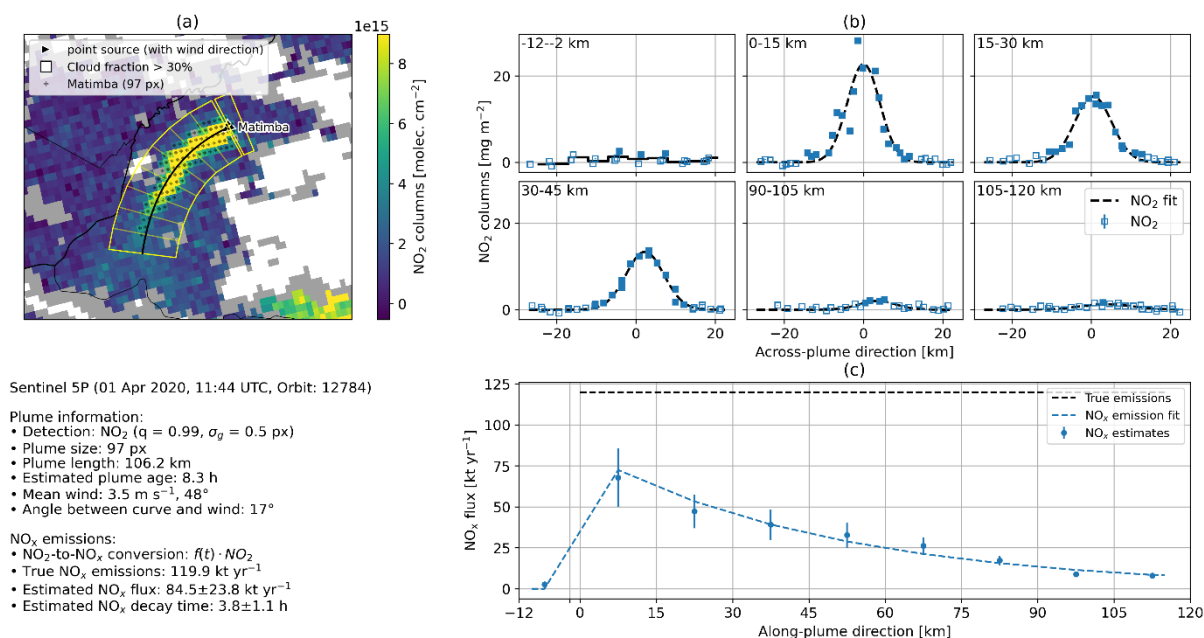
Figure 2.1: Example of the NO_x emission estimate using the cross-sectional flux method implemented in *ddeq*.

3 Data

3.1 MicroHH simulations

To gain a better understanding of the NO_x:NO_2 ratios in plumes, model simulations from the library of plumes can be analysed (see section 2.1). Koene and Brunner (2023) made a comparison between the library of plumes and available observational data for these simulated plumes. They found that the highest resolution model MicroHH was able to simulate the plumes most realistically, although there was a slight tendency to underestimate the plume width in most simulations. MicroHH is an open-source numerical fluid dynamics model for simulating turbulent flows in the atmosphere (van Heerwaarden et al., 2017) and can be coupled with chemistry schemes (Krol and Van Stratum, 2021). For the $CoCO_2$ project, large-eddy simulations (LES) were run in combination with a simplified version of the chemistry scheme used in the IFS (Huijnen et al., 2016). The chemistry scheme included the reactive species O_3, NO, NO_2, NO_3, N_2O_5, HNO_3, CO, CH_4 (fixed), H_2 (fixed), HO_2, OH, H_2O_2, CH_2O, RO_2, and $ROOH$, as well as C_3H_6 as a representative of VOCs. The chemistry was tuned to match the NO_x and HO_x chemistry of the IFS and to realistically represent the photo-stationary state between NO_x and O_3. The specific model settings and boundary conditions used for the MicroHH model runs are described in Krol and Van Stratum (2021) as well as Koene and Brunner (2023) and are briefly summarised below.

The MicroHH model was run on a 128 x 128 x 4 km domain for Matimba and a 51.2 x 51.2 x 4 km domain for Bełchatów, Jänschwalde, and Lipetsk (Figure 3.1). The spatial resolution was set to 100 x 100 x 25 m for the Matimba case and 50 x 50 x 25 m for the others (Koene and Brunner, 2023). Each case was simulated for 48 hours, starting at 00:00 UTC, and the output was saved hourly. The model was initialised and driven with hourly meteorological data from the ERA5 reanalysis dataset (see section 3.3). For the background concentrations of trace gases, reanalysis data from the Copernicus Atmosphere Monitoring Service (CAMS) were used (Koene and Brunner, 2023). To simulate the plumes, typical quantities
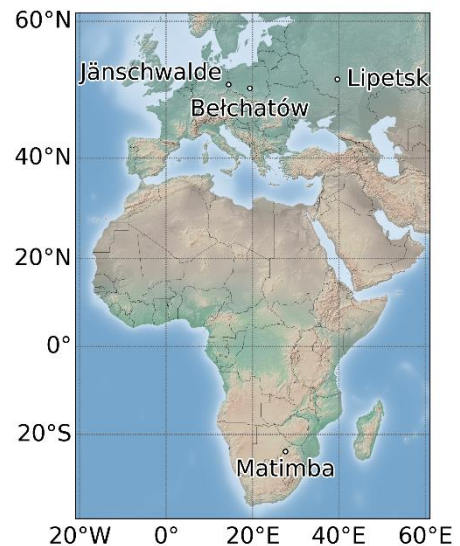
Figure 3.1: Location of the four MicroHH simulations Bełchatów (PL), Jänschwalde (DE), Lipetsk (RU), and Matimba (ZA).

of CO_2 and NO_x emissions from bottom-up reported values of previous years were released at the respective locations of the power plants and industrial facilities (Table 3.1) (Krol and Van

Stratum, 2021). However, for the Matimba simulation, the prescribed emissions did not include emissions from the Medupi power plant (Koene and Brunner, 2023). To realistically simulate NO_x chemistry, the NO_x emissions were split into 95% NO and 5% NO_2 by mass (Koene and Brunner, 2023). Due to an error in the MicroHH simulation runs, the actual prescribed emissions were higher than described in Krol and Van Stratum (2021).

Table 3.1: Details of the four MicroHH simulations and the prescribed CO_2 and NO_x emissions from bottom-up reported emissions which have been corrected for the error in the simulations (Krol and Van Stratum, 2021).

Source	Coordinates	Simulation Period	CO_2 emissions [kg/s]	NO_x emissions [kg/s]
Bełchatów (PL)	19.33°E 51.27°N	06-07 June 2018	1375.9	1.0777
Jänschwalde (DE)	14.46°E 51.84°N	22-23 May 2018	853.7	0.7017
Lipetsk (RU)	39.62°E 52.56°N	12-13 June 2019	1165.5	0.9543
Matimba (ZA)	27.61°E 23.67°S	24-25 July 2020	1014.0	2.6480

As flue gases rise due to buoyancy, the simulations were run three times for each source with different emission height profiles: Surface release, middle release, and high release. Each case was intended to reflect different atmospheric conditions. The corresponding vertical emission profiles were calculated based on the stack height and plume rise calculations. These incorporated the flue gas temperatures as well as atmospheric stability and wind speeds (Koene and Brunner, 2023). For the current study, only the middle release scenario (*_M) was used as it corresponds to the expected conditions.

The model output consists of 3D data of the reactive trace gases and CO_2 as well as meteorological variables such as temperature, pressure, and wind speed. The output was post-processed into 2D datasets resembling synthetic satellite observations. The resolution was degraded to the expected resolution of the CO2M satellites of 2 × 2 km. For the wind speeds, a 2D weighted average of the 3D wind fields was calculated based on the vertical emission profile. The details of the post-processing are described in Koene and Brunner (2023).

3.2   TROPOMI

The method of converting NO_2 to NO_x developed in the current study is applied to TROPOMI NO_2 observations as a case study. The data can be obtained in full orbits from the Sentinel-5P Pre-Operations Data Hub (https://s5phub.copernicus.eu/) or via Application Programming

Interface (API) (Copernicus Sentinel-5P, 2021). For this purpose, the Python package *sentinel-sat* was used to acquire the latest processing version, v2.4.0, of the NO_2 level 2 data product which has been operational since July 2022. Earlier data since the end of April 2018 have been reprocessed to version 2.4.0 and are available as S5P_RPRO (Eskes and Eichmann, 2023). As the spatial resolution of TROPOMI has improved since August 2019 (see section 2.5), only data for the years 2020 and 2021 were used in this study. In accordance with van Geffen et al. (2019), only data with quality assurance values higher than 0.75 were utilised. In addition, the auxiliary data comprising 3D NO_2 fields from the TM5-MP model were downloaded to recompute the AMFs (Eskes and van Geffen, 2021).

3.3 ERA5 reanalysis

The cross-sectional flux method requires wind data to convert trace gas line densities into fluxes. For this purpose, data from the ERA5 reanalysis dataset were used. ERA5 is the latest generation of ECMWF's global reanalysis which assimilates a range of observations of atmospheric, oceanic and land parameters into a numerical model. The model simulates the parameters with seamless spatial coverage and produces hourly outputs with a spatial resolution of $0.25° \times 0.25°$ on 137 model levels up to 80 km. The data can then be obtained at single, pressure, and model levels (Copernicus Climate Change Service and Climate Data Store, 2023; Hersbach et al., 2023).

For this study, the zonal and meridional wind speed components u and v [m/s], temperature t [K] and specific humidity q [kg/kg] were obtained on the model levels 100 to 137, the latter being the lowest model level. In addition, the natural logarithm of the surface pressure $lnsp$ [-] was queried as a single level variable. Similarly, the (planetary) boundary layer height blh [m] was obtained. All variables were acquired using an API provided by ECMWF in the Python package *cdsapi* (Copernicus Climate Change Service and Climate Data Store, 2023).

3.4 Bottom-up reported NO_x emissions

Bottom-up reported emissions are needed to assess the accuracy of emission estimates. Since the year 2000, member states of the European Union have been required to report their emissions of air and water pollutants (European Parliament and Council of the European Union, 2006). These data were made publicly available in 2006 through the European Pollutant Release and Transfer Register (E-PRTR). The database contains the annual emissions of pollutants from

nine major sectors such as energy production or metal processing and is available on the European Industrial Emissions Portal (https://industry.eea.europa.eu/).

For this study, data on annual NO_x emissions from the Jänschwalde power plant were downloaded for the years 2020 to 2021. For the Bełchatów power plant, the data are only available up to 2017. Therefore, the CO_2 and NO_x emissions for 2017 were used to extrapolate the expected emissions for the years 2020 to 2021 (see section 4.8).

For the metallurgical plant in Lipetsk, pollutant emissions are included in the annual report of the operating company NLMK (https://nlmk.com/en/ir/results/annual-reports/). However, emissions for this site are only reported in kilograms per tonne of steel produced. As there is no indication of the total amount of steel produced at the Lipetsk site, the NO_x data could not be converted into total emissions. As a result, the prescribed emissions of NO_x, CO_2 and CO in the MicroHH simulations did not represent the Lipetsk site in particular but rather the NLMK group as a whole. In addition, NLMK produces electricity in captive power plants at the Lipetsk site (NLMK Group, 2021). However, it is unclear whether these NO_x emissions are included in the reported emissions. Therefore, this study does not use bottom-up reported emission data for Lipetsk.

For the Matimba and Medupi power plants, daily emissions are provided in monthly reports by the operating company Eskom (https://www.eskom.co.za/dataportal/emissions/ael). The NO_x emission data for the years 2020 and 2021 were collected and summed for both power plants. For 2022, not all data was available at the time of the analysis which is why the focus of this study lies on the years 2020 and 2021.

3.5 Energy generation

To interpolate the monthly or annual bottom-up reported CO_2 and NO_x emissions of power plants to a higher temporal resolution, their energy output can be used (Nassar et al., 2022). For European power plants, the amount of electricity generated is available at hourly resolution on the transparency platform of the European Network of Transmission System Operators for Electricity (ENTSO-E) (https://transparency.entsoe.eu/).

For this study, data of the Bełchatów and Jänschwalde power plants for the years 2017, 2020 and 2021 were retrieved via an API using the Python package *entsoe-py*. For the Matimba and Medupi power plants, the daily electricity production is provided in the monthly reports of the operating company Eskom.

4 Methods

4.1 Analysis of NO_x:NO_2 ratios

In order to implement a more realistic conversion of NO_2 to NO_x, the vertically integrated MicroHH simulations were analysed for the sources Bełchatów, Jänschwalde, Lipetsk, and Matimba (see section 3.1).

As a first step, the plume detection and centre line fit from *ddeq* were applied to all but the first time step at 00:00 UTC, as it was the initialisation of the model run. For some time steps this procedure failed because the plume was outside the model boundaries, or the analytical solution of the centre line fit had multiple solutions. Consequently, these time steps were omitted. When the centre line was successfully fitted, polygons with a length spacing of 5 km were computed along the centre line. For each polygon, the line densities of CO_2, NO, and NO_2 were calculated by summing the concentration of each pixel within the polygon. The sums were multiplied by the pixel size and divided by the length of the polygon to obtain the line densities. The concentrations were given as the sum of the background and power plant concentrations of the middle emission profile. Contrary to the procedure in *ddeq*, where a Gaussian curve is fitted to the VCDs of every pixel in each polygon to estimate the line densities, the concentrations were summed because no clouds were simulated in MicroHH. Therefore, the simulated trace gas fields had no missing values that could have biased the integration.

The NO_x columns were calculated by adding the summed NO and NO_2 columns and the NO_x:NO_2 ratios were computed for each polygon along the plume.

4.2 Calculation of representative wind speeds

The conversion of trace gas line densities into fluxes using the cross-sectional flux method requires the wind speed at which the plume is transported (see section 2.6). While the plume is advected at different speeds at different altitudes, satellites measure a vertically integrated 2D representation of the plume. Accordingly, a 2D wind field must be calculated that is representative of the effective wind speed at which the plume was transported. In the current study, two methods were implemented.

One method to calculate such a vertically integrated wind is to weight the ERA5 3D wind fields with a profile representing the expected vertical distribution of emissions in Figure 4.1 (Brunner et al., 2019). In this study, it is referred to as the GNFR-A profile as it represents the emission

profile of the public electricity and heat generation which belong to the category A of the Gridded Nomenclature For Reporting (GNFR) framework (UNECE, 2015).

In order to weight the 3D wind fields with the profile, the first step was to calculate the geometric height of the ERA5 model layers which was done according to the ERA5 documentation (Copernicus Climate Change Service and Climate Data Store, 2023). For this purpose, the pressure at each model half layer was calculated using the coefficients a_b and b_b defining the model layer boundaries and the surface pressure $p_s = e^{lnsp}$:
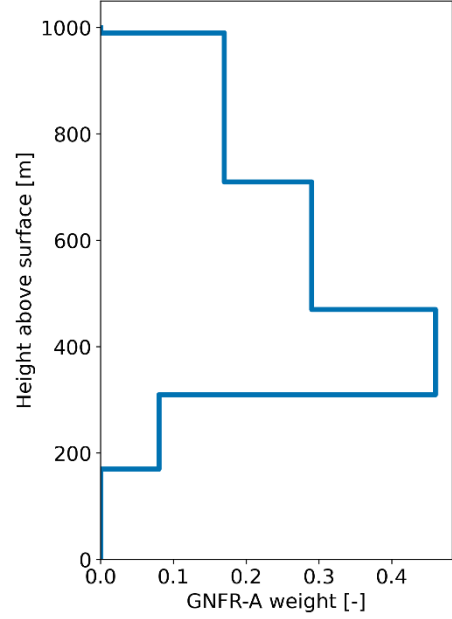
Figure 4.1: GNFR-A profile as a function of height.

$$p_b = a_b + b_b \cdot p_s \tag{4.1}$$

The pressure in the middle of the layers was calculated by averaging the pressure at the upper and lower boundaries of each layer:

$$p_l = \frac{p_{b,top} + p_{b,bottom}}{2} \tag{4.2}$$

The virtual temperature of each layer $T_{v,l}$ was calculated using the temperature T_l and specific humidity q_l of each layer (Lohmann et al., 2016):

$$T_{v,l} = T_l \cdot (1 + 0.608 \cdot q_l) \tag{4.3}$$

Finally, the height of each layer was calculated using the hypsometric equation (Wallace and Hobbs, 2006):

$$h_l = \ln\left(\frac{p_s}{p_l}\right) \cdot \frac{R \cdot T_{v,l}}{m \cdot g} \tag{4.4}$$

where R is the universal gas constant and $m = 0.02896$ kg/mol is the molar mass of dry air.

The GNFR-A profile weights were interpolated to the geometric height of the ERA5 model layers and normalised by dividing the weight of each layer by the sum of all weights. The horizontal components of the wind speed (u, v) were then multiplied by the corresponding weight, summed over each layer, and divided by the vertical sum of the weights.

A second method of calculating a vertically integrated wind describing the advection of a plume is to calculate the mean wind speed within the planetary boundary layer (PBL). For this, the

geometric height of each ERA5 model layer was calculated analogously to the first method above and the unweighted mean wind speed within the PBL was calculated. If the PBL was lower than the mode of the GNFR-A emission profile, the wind speed was omitted. The threshold was set at 400 m, but should ideally be dynamic and take into account parameters such as stack height, flue gas properties, and meteorological conditions (Brunner et al., 2019).

However, computing accurate PBL-averaged wind speeds was beyond the scope of this study. Therefore, the GNFR-A weighted wind speeds were used for estimating NO_x emissions from TROPOMI images.

As in Kuhlmann et al. (2021), a fixed uncertainty was assumed for the wind speed. This value was set to 1 m/s even though Gualtieri (2022) estimated the total systematic uncertainty of the ERA5 wind data to be about -0.1 m/s compared to observations. The more conservative estimate of 1 m/s is intended to incorporate the uncertainty due to vertical averaging of 3D wind fields.

4.3 Backward integration of wind speed

When computing the NO_x:NO_2 ratios following the method explained in section 4.1, the ratios are given as a function of distance along the plume, which is strongly dependent on the prevailing wind speeds. However, as seen in section 2.4, the extent to which NO_x chemistry has progressed depends on the time since emission. Thus, the NO_x:NO_2 ratio must be expressed as a function of time since emission by dividing the distance along the plume by the wind speed.

As the wind speed varies over time, sections of the plume that are now downstream were possibly emitted at different wind speeds that the wind speed at the time of satellite overpass. Accordingly, to properly convert the distance along the plume into time since emission, the wind speed history has to be taken into account. To approximate it, the wind speed was iteratively integrated backwards in time along the plume. For MicroHH, the modelled winds were employed while for TROPOMI images, ERA5 wind data was utilised. In a first step, the wind speed at the source at time t was multiplied by one hour to calculate the distance d_t along the plume which an air parcel would have travelled in that time. In a second step, the wind speed at the source at time $t-1$ was used to calculate d_{t-1}. The resulting distance was added to d_t to estimate the total distance travelled by an air parcel that was emitted an hour prior. This process was repeated until the cumulative distance was greater than the detected plume. The result was the wind speeds of the past time steps representing the cumulative distance along the

plume. These wind speeds were then interpolated to the distance along the plume at the centre of each polygon.

To test whether the backward integration of wind speeds is a good representation of the effective wind speed in the plume, the Pearson correlation coefficient between the CO_2 line densities and the wind speed of each polygon was calculated for all time steps of the four MicroHH simulations. The CO_2 line densities were used to avoid a confounding influence of chemistry on the correlation coefficient. The above procedure was performed once using only the wind speed at the source for each time step and once using the backward integrated wind.

4.4 Conversion of NO_2 to NO_x

To obtain a NO_2-to-NO_x conversion factor for each of the four sources, the median and standard deviation of the NO_x:NO_2 ratios calculated in section 4.1 were used. Only the time steps 8 to 14 UTC during the day were used because the PBL starts to shrink in the afternoon. The plume is thus emitted into the free troposphere and experiences a different wind speed than the part of the plume that was previously emitted into the PBL. Additionally, air parcels which were previously within the PBL become part of the free troposphere where wind speeds are higher and often differ in direction compared to the PBL winds. The different directions of propagation result in two plumes which can lead to the failure of the centre line fit. The different wind speeds cause secondary NO_x peaks which often lead to inaccurate emission estimates when fitting the trace gas flux along the plume. Furthermore, using only daytime simulations ensures that the NO_2-to-NO_x conversion factors are fitted under similar conditions as at the time of the TROPOMI overpass.

A negative exponential function was fitted to the median NO_x:NO_2 ratio of each source, using the standard deviation as the weight for the fit:

$$f(t) = m \cdot e^{-\tau \cdot t} + f_0 \qquad (4.5)$$

Ther fitting parameter m represents the scaling factor, τ the decay constant and f_0 the offset term to which the NO_x:NO_2 ratio will converge to.

The resulting conversion factor $f(t)$ can be multiplied by the corresponding NO_2 line densities to obtain NO_x. The uncertainty σ_f of f is calculated according to the propagation of uncertainty:

$$\sigma_f = \sqrt{\left(\frac{\delta f(t)}{\delta m}\right)^2 \cdot \sigma_m^2 + \left(\frac{\delta f(t)}{\delta \tau}\right)^2 \cdot \sigma_\tau^2 + \left(\frac{\delta f(t)}{\delta f_0}\right)^2 \cdot \sigma_{f_0}^2} \qquad (4.6)$$

The uncertainty σ_f is used to update the uncertainty σ_l of the NO$_x$ line densities l:

$$\sigma_l = \sqrt{f^2 \cdot \sigma_l^2 + \sigma_f^2 \cdot l^2} \qquad (4.7)$$

In an exploratory approach, a simple random forest (RF) regression was tested to obtain an estimate of the fit parameters m, τ and f_0 that can account for different locations and conditions. Therefore, Eq. (2.5) was fitted to the NO$_x$:NO$_2$ ratios of each time step of the four simulated cases. The fitted parameters were used as response variables in the RF, while the solar zenith angle (SZA), temperature, prescribed emissions, and the background (BG) concentrations of the trace gases in the MicroHH simulations served as explanatory variables. The SZA was used as a proxy for the photolysis rate because they are linearly correlated but the SZA is easier to calculate. The RF consisted of 1000 trees, each using a random selection of only three explanatory variables.

4.5 Validation of the NO$_2$-to-NO$_x$ conversion

To ensure that the algorithm described in the previous section yields NO$_x$ emission estimates that are consistent with the emitted quantities, the algorithm was tested using the same MicroHH data that was employed to calculate the NO$_2$-to-NO$_x$ conversion. For this purpose, the NO$_x$ emissions of the same daytime time steps as in section 4.4 were estimated three times with *ddeq*: once using the modelled NO$_x$ fields, once using the NO$_2$ fields and applying the constant NO$_2$-to-NO$_x$ conversion factor of 1.32 (referred to as the old algorithm), and once using the negative exponential functions fitted in section 4.4 as conversion factors (referred to as the new algorithm).

To separate the effects of the newly implemented NO$_2$-to-NO$_x$ conversion and the backward integrated winds, this validation was performed once using only the wind speed at the source for the whole plume and once using the backward integrated wind.

The quantified NO$_x$ emissions were compared to the prescribed (i.e., true) emissions in the model runs. In addition, the NO$_x$ decay time was used to assess whether the new algorithm provides a more realistic representation of NO$_x$ chemistry.

4.6 Processing of TROPOMI datasets

The downloaded NO$_2$ and auxiliary TROPOMI data were combined into one dataset, cropped to the respective sources, and some variables were renamed to ensure compatibility with the existing algorithms in *ddeq*.

The uncertainty of the tropospheric NO$_2$ VCDs was set to $7.6 \cdot 10^{-7}$ kg/m^2, which corresponds to $1 \cdot 10^{15}$ molecules/cm^2. This is an average uncertainty over polluted regions and corresponds to approximately 20% of the measured NO$_2$ VCDs (van Geffen et al., 2019). The constant uncertainty was used over the tropospheric NO$_2$ VCD precision in the TROPOMI data file, as the latter depends on the slant column density and thus on the VCD itself (see also Kuhlmann et al. (2022)).

4.7 Calculation of the updated air mass factor

As the TM5-MP model has a relatively coarse resolution of $1° \times 1°$, it cannot resolve individual plumes. Therefore, the NO$_2$ profiles in these areas are underestimated which leads to biases in the AMFs and VCDs (see section 2.5). To evaluate the influence of the NO$_2$ profile on the tropospheric AMFs and VCDs, both were recalculated exploratively for Matimba, using the higher resolution MicroHH profiles. In a first step, the pressure of each model level of the TROPOMI auxiliary data was calculated using Eq. (4.1), where the parameters a_m and b_m were given for the centre of each TM5-MP model layer. Consequently, the application of Eq. (4.2) was omitted. In a second step, the geometric height of each TM5-MP model layer was calculated by applying Eq. (4.4). However, instead of the virtual temperature, the air temperature was used because no measure of humidity is given in the auxiliary data. In a third step, the TM5-MP latitude and longitude were interpolated to the TROPOMI NO$_2$ product and the two datasets were merged. Next, the MicroHH NO$_2$ profiles of the Matimba model domain were interpolated to the heights of the TM5-MP model. Below a height of 4 km, where MicroHH data are available, the TM5-MP profile was replaced by these profiles. Finally, the new AMFs were calculated using the averaging kernels A_l and the new NO$_2$ concentrations in each layer $x_{new,l}$ (Eskes et al., 2022):

$$AMF_{new}(x_{new}) = AMF_{old}(x_{old}) \cdot \frac{\sum_l A_l \cdot x_{new,l}}{\sum_l x_{new,l}} \tag{4.8}$$

The updated AMFs were then used to update the VCDs:

$$VCD_{new} = \frac{VCD_{old} \cdot AMF_{old}}{AMF_{new}} \qquad (4.9)$$

In the above approach, the NO_2 profiles were replaced up to a height of 4 km. However, it is in fact only necessary to update the profile within the PBL, as NO_2 is emitted into the PBL, leading to greater spatial heterogeneity there.

To investigate the effects of higher NO_2 concentrations in the PBL on the AMFs for the TROPOMI images of Bełchatów, Jänschwalde, Lipetsk, and Matimba, the ERA5 PBL height data were interpolated to the higher resolution TROPOMI pixels. The NO_2 concentration within the PBL of the detected plumes was set to $5 \cdot 10^{-9}$ mol/mol for all images of the years 2020 and 2021. This is a representative NO_2 concentration for the plumes based on the four MicroHH simulations. With these profiles, the new AMFs were calculated using Eq. (4.8) and compared with the existing ones.

Ideally, the NO_2 profiles of the background pixels should also be updated using concentrations from higher resolution models. However, the temporally and spatially varying background conditions make it difficult to estimate representative background concentrations for annual data at different locations. Therefore, the NO_2 profiles within and outside the detected plume were only exploratively updated. This was done for the TROPOMI image of Matimba on the 25th of July 2020 at 12:00 UTC as it corresponds to the date of the MicroHH simulation. The PBL NO_2 profiles within the detected plume were set to $5 \cdot 10^{-9}$ mol/mol and outside of the plume to $2 \cdot 10^{-10}$ mol/mol. Both values are representative concentrations within the PBL in the MicroHH simulations. The AMFs and VCDs were recalculated using Eqs. (4.8) and (4.9) and used to estimate the NO_x emissions.

Updating the NO_2 concentration within the PBL to a fixed value is problematic as the concentration depends, among other things, on source strength and wind speed. Applying the same PBL concentration to different plumes is therefore not advisable. For this reason, the current study includes an exploratory approach to iteratively update the NO_2 profiles within the PBL by using a first estimate of the NO_x emissions. To do so, a relationship must be derived between the total NO_x mass in a plume and the median wind speed within the plume. This was done by summing the NO_x VCDs of the entire detected plume in each time step of each MicroHH simulation. The sum was then multiplied by the pixel size to obtain the total NO_x mass of the plume. As the models had different prescribed emissions and the plumes had different lengths in each time step, the result was corrected by dividing the NO_x mass by emission strength and plume length, yielding the corrected NO_x mass. In addition, the median wind speed of the plume was

calculated. The function in Eq. (4.10) was fitted to the relationship between the median wind speed w and the corrected NO_x mass m.

$$m(w) = a \cdot w^b \tag{4.10}$$

From this relationship, the expected corrected NO_x mass in a plume can be estimated for a given wind speed. Multiplying the NO_x mass by the length of the plume as well as the first NO_x emission estimate and distributing the resulting mass equally into each polygon along the plume gives an estimate of the average NO_x mass in each polygon. By dividing this value by the number of plume pixels detected in each polygon and the area of each pixel, the average VCD of all pixels can be calculated. It can be converted to an average NO_x profile within the PBL by dividing by the PBL height. To convert to NO_2, the values are divided by 1.5, which is the average of the fitted values for f_0 in section 4.4. Estimating the NO_2 concentration within the PBL iteratively was performed exploratively for the Matimba simulation on the 25th of July 2020 at 12:00 UTC.

4.8 Interpolation of bottom-up reported NO_x emissions

According to Nassar et al. (2022), the monthly and annual bottom-up reported CO_2 and NO_x emissions of power plants can be interpolated to a higher temporal resolution using their energy output. In a first step, the generated power of each operating unit was summed. The hourly or daily output of each year was divided by the average output of that year. Finally, the resulting values were multiplied by the monthly or annual bottom-up reported emissions and converted to kilotons per year.

For Bełchatów, data for CO_2 and NO_x emissions are only available until 2017. To obtain estimates for the years 2020 to 2021, the power output for each year was summed and divided by the sum of the year 2017. These values were then multiplied by the CO_2 and NO_x emissions of the year 2017 to get the estimated emissions for each year. Finally, the annual emissions were interpolated using the same procedure as above. To check the plausibility of the extrapolated values for Bełchatów, the expected CO_2 emissions were compared with those in Table 1 of Nassar et al. (2022).

4.9   Application of the NO₂-to-NOₓ conversion to TROPOMI

From the downloaded and processed TROPOMI data, those with missing values around the source and those with non-visible plumes were discarded. For the remaining data, the cross-sectional flux method was applied. Images where other plumes were erroneously detected, where the fitted curve did not accurately represent the plume, where the NOₓ fluxes along the plume had outliers, or where the wind direction deviated more than 90° from the plume were removed. To ensure that there were enough pixels to reliably fit a Gaussian curve of NO₂ VCDs in each polygon, the polygon spacing was set to 15 km. For each image, ERA5 wind data were processed as described in sections 4.2 and 4.3. Emissions were estimated using the old and new algorithms and the AMF correction was applied to the latter. For each source, the respective fitting parameters in Table 5.1 were used to convert NO₂ into NOₓ.

When calculating the annual statistics of the estimated NOₓ emissions, the median and standard deviation were calculated as the median of the monthly statistics. This was done to avoid a potential bias due to an unbalanced number of data points for each month. For the uncertainty of the annual emission estimates, a seasonal cycle was fitted to the emission estimates using a cubic Hermite spline with periodic boundary conditions (Kuhlmann et al., 2021). The corresponding uncertainty σ_e accounts for the uncertainties of the single-overpass estimates through error propagation. To further account for uncertainties in the diurnal (σ_d) and seasonal (σ_s) cycles, the total uncertainty σ_{tot} was calculated as follows:

$$\sigma_{tot} = \sqrt{\sigma_e^2 + \frac{\sigma_d^2}{n} + \frac{\sigma_s^2}{n}} \qquad (4.11)$$

Here, both σ_d and σ_s were set to 30% according to Hill and Nassar (2019).

As the estimated NOₓ emissions with the new algorithm depend on the NO₂-to-NOₓ conversion factor, a sensitivity analysis was performed by applying the NO₂-to-NOₓ conversion factors of Jänschwalde and Matimba calculated in section 4.4 to all four sources.

5 Results

5.1 Analysis of $NO_x:NO_2$ ratios

The analysis of the $NO_x:NO_2$ ratios in the MicroHH model runs for Bełchatów, Jänschwalde, Lipetsk, and Matimba in Figure 5.1 confirms that the $NO_x:NO_2$ ratios strongly depend on the time of day as well as on the time since emission: They reach the highest values at night and close to the source while the lowest values are observed in the afternoon and far from the source. The 1st to 99th percentiles range from 1 to 14. It is important to note that the time steps of the model run on the y-axis are shown in UTC whereas the local time would be UTC+2 for all four cases.
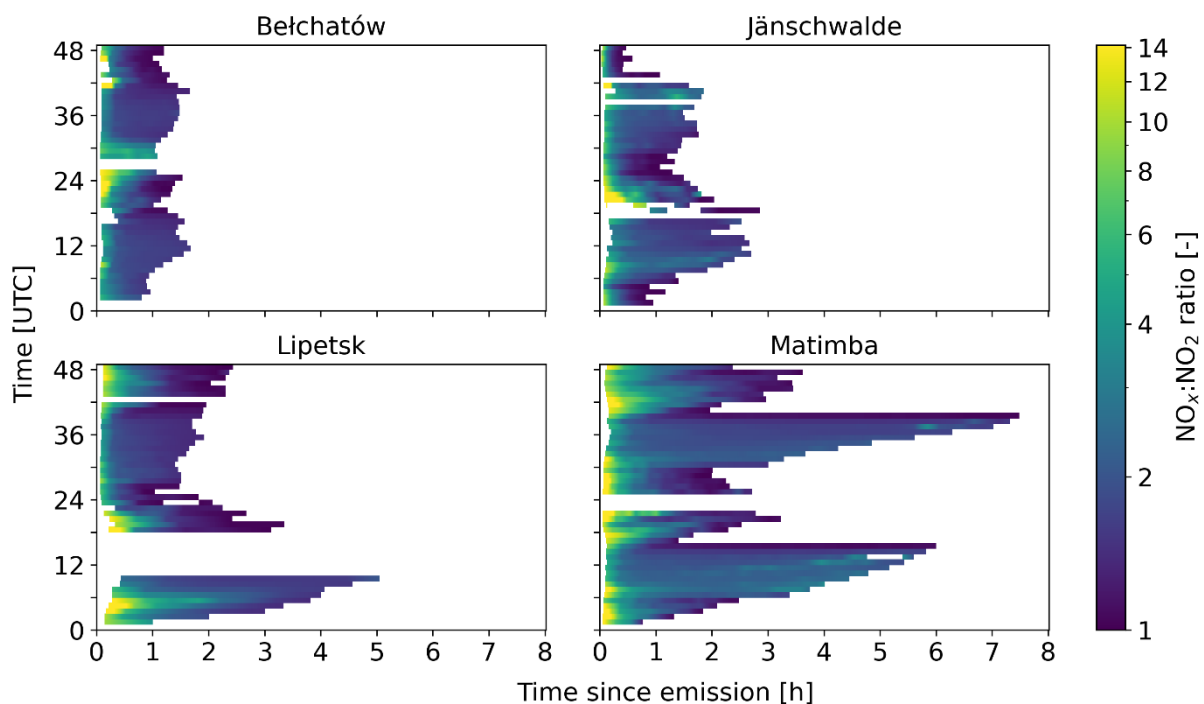
Figure 5.1: $NO_x:NO_2$ ratios for the 48 time steps of the MicroHH simulations of Bełchatów, Jänschwalde, Lipetsk, and Matimba as a function of time since emission.

The $NO_x:NO_2$ ratios of the Matimba model run are comparatively higher both at the source and at the tail of the plume compared to the other three simulations. Furthermore, the plumes in the Matimba simulation were much longer than those in Bełchatów, Jänschwalde, and Lipetsk, due to the smaller model domains for the latter three. Consequently, the time since emission is shorter for these cases.

5.2 Calculation of representative wind speeds

As described in section 4.2, the GNFR-A weighted and mean PBL winds were implemented in this study to calculate 2D horizontal wind speeds from the ERA5 3D wind fields. However, the analysis of the resulting wind speeds showed only minor differences in most cases. An example for the 29th of May 2020 at 11:00 UTC for the location of Matimba is depicted in Figure 5.2. It shows that the GNFR-A profile in (a) lies entirely within the PBL which explains the good agreement between the 2D wind speed in black.
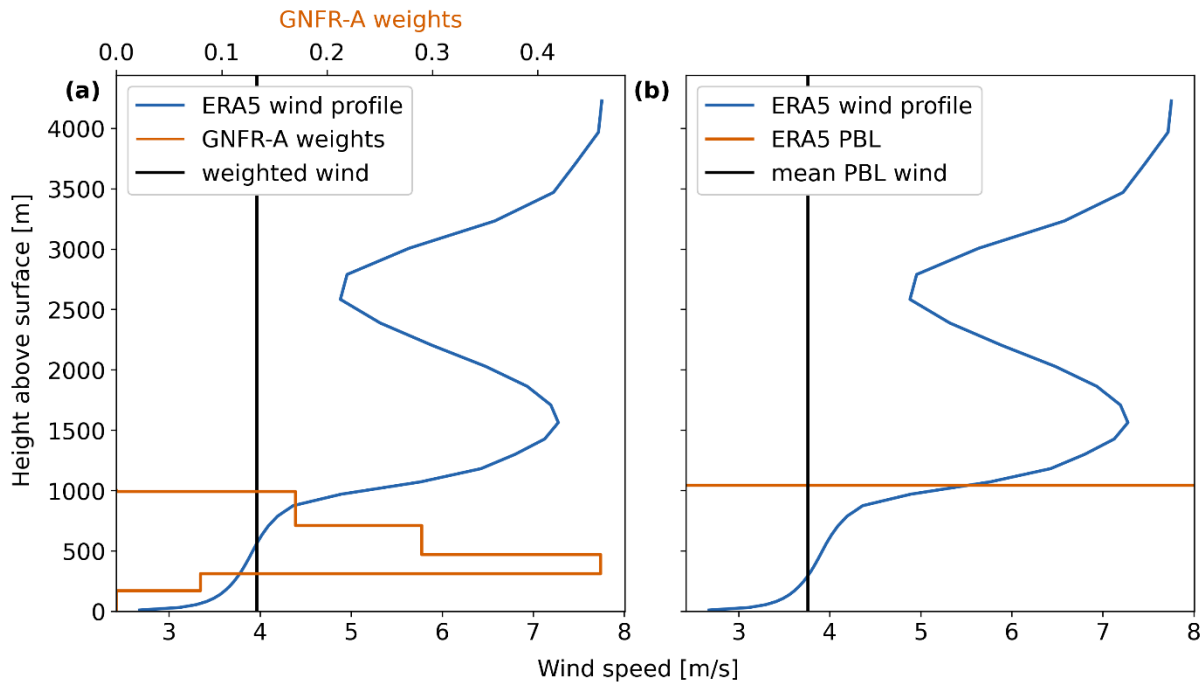
Figure 5.2: Calculation of a representative wind speed from an ERA5 wind profile for the location of Matimba on the 29th of May 2020 at 11:00 UTC. (a) Weighted wind using the GNFR-A profile. (b) Mean wind within the planetary boundary layer (PBL).

The vertically averaged wind speeds deviate more when the PBL is shallower, which is the case in the morning and in winter. In some cases, the PBL may also be below the stack height of the sources. For this reason, the GNFR-A weighted wind speeds have been used in this study as described in section 4.2.

5.3 Backward integration of wind speed

The correlation between the CO_2 line densities and the two representations of wind speed in each polygon is shown in Figure 5.3. At the source, the correlation is strongly negative but weakens for both representations of wind speed further away from the source. However, the correlation remains stronger for the backward integrated wind speeds compared to using only the wind at the source. This is especially the case for the long plumes of the Matimba simulation.
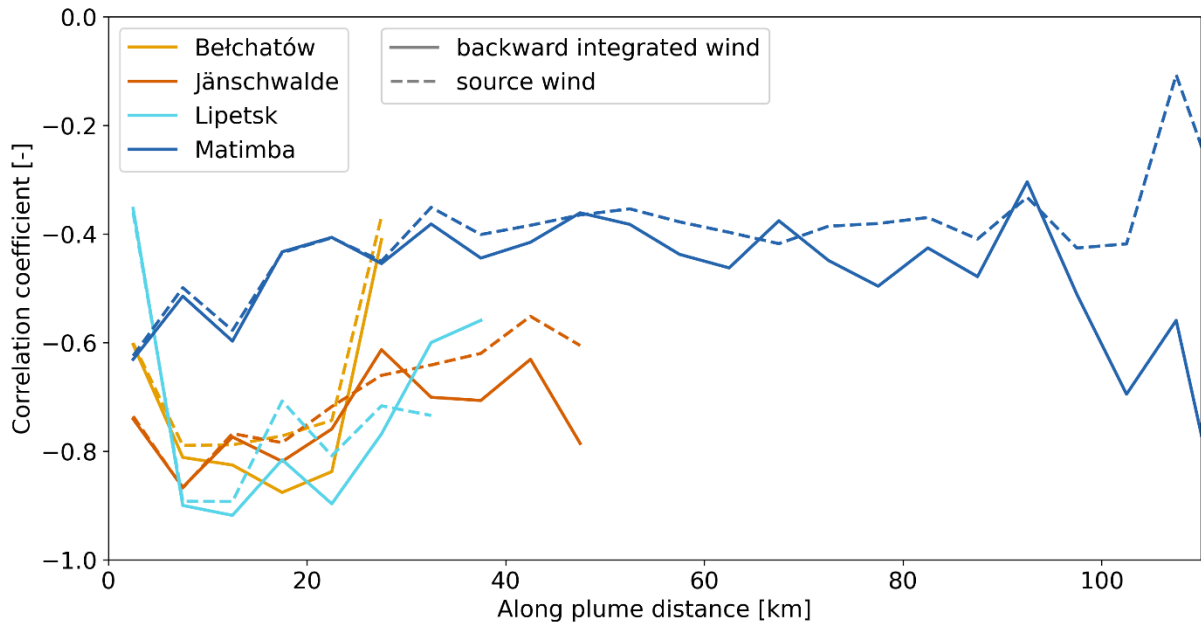
Figure 5.3: Pearson correlation coefficient between CO_2 line density and wind speed in each polygon of the detected plumes of the MicroHH simulations of Bełchatów, Jänschwalde, Lipetsk, and Matimba.

5.4 Conversion of NO_2 to NO_x

Figure 5.4 shows the NO_x:NO_2 ratios of the daytime time steps 8 to 14 for both simulated days of all four model simulations. Plot (a) depicts the median and standard deviation of the ratios, while (b) shows the corresponding fitted negative exponential functions.
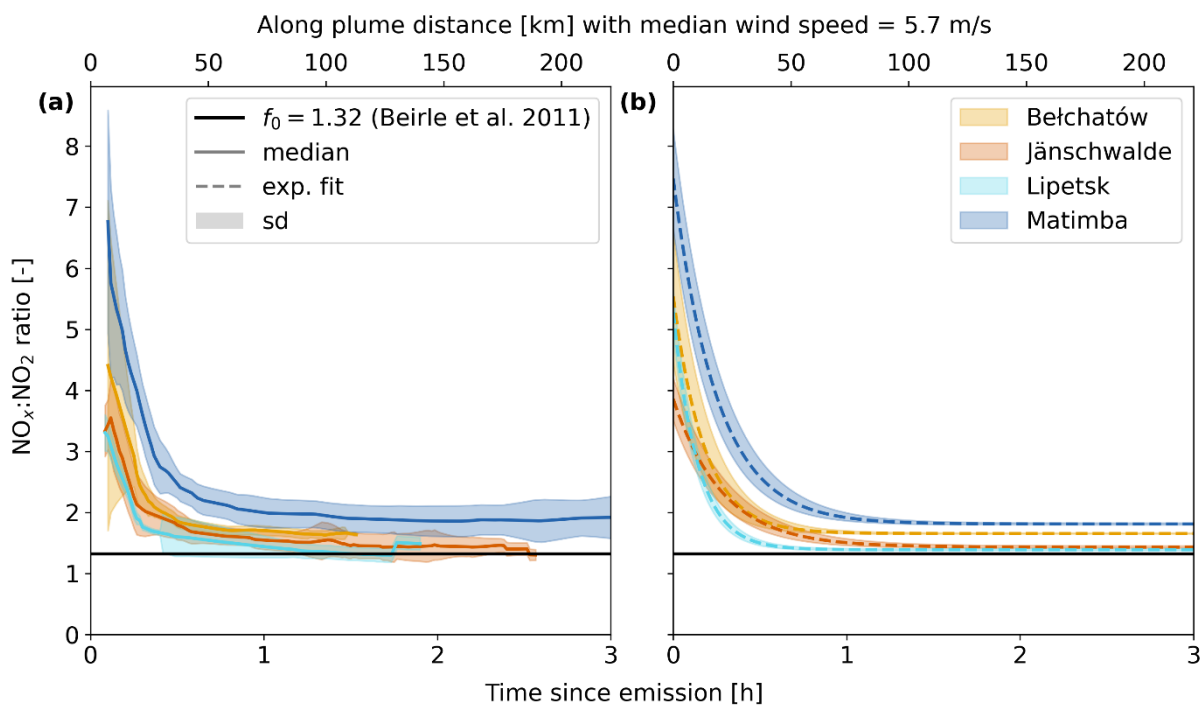
Figure 5.4: NO_x:NO_2 ratios of the MicroHH daytime time steps as a function of time since emission. (a) Median and standard deviation. (b) Fitted negative exponential function and corresponding standard deviation.

The corresponding fitting parameters are listed in Table 5.1.

Table 5.1: Fitting parameters of the negative exponential function in (4.5) for the daytime values of the NO_x:NO_2 ratios of the four MicroHH simulations.

Source	$m\ [-]$	$10^3 \cdot \tau\ [1/s]$	$1/\tau\ [\mathrm{min}]$	$f_0\ [-]$
Bełchatów	3.89 ± 1.07	1.56 ± 0.18	10.67	1.65 ± 0.00
Jänschwalde	2.43 ± 0.33	0.98 ± 0.10	17.05	1.43 ± 0.02
Lipetsk	3.90 ± 0.34	1.99 ± 0.10	8.38	1.39 ± 0.01
Matimba	5.66 ± 0.80	1.11 ± 0.01	15.08	1.81 ± 0.01

Similar to Figure 5.1, Figure 5.4 reveals that the NO_x:NO_2 ratio is much higher than the previously used conversion factor $f_0 = 1.32$ in black (see section 2.4). However, the Jänschwalde and Lipetsk simulations approach this value after one hour. On the contrary, the NO_x:NO_2 ratios of Bełchatów and Matimba show a significant deviation from 1.32. In all four simulations, the ratios level off half an hour after the emission or 50 km along the plume. Furthermore, Figure 5.4 illustrates that the standard deviation close to the source is largest for Bełchatów, which leads to a higher uncertainty in the fitted function.

The results of the exploratory RF regression in Figure 5.5 show that photolysis rates (represented by SZA), air temperature, prescribed emissions and CO background concentrations were most important in predicting the fitting parameters.
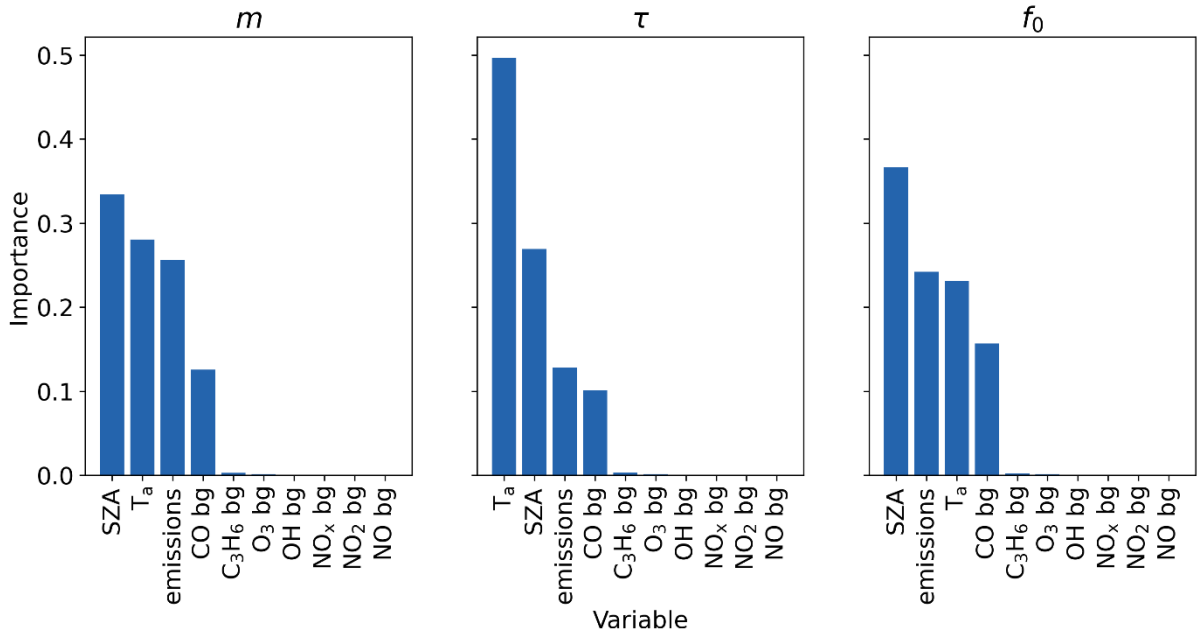
Figure 5.5: Importance of the explanatory variables predicting the fitting parameters m, τ and f_0 using a random forest.

Using this RF to predict the fitting parameters for estimating NO_x emissions revealed that the median estimated emissions were comparable to those using the simulation specific conversion

factors in Table 5.1. However, the variability of the emission estimates was much higher using the RF.

5.5 Validation of the NO₂-to-NOₓ conversion

The application of the new algorithm to MicroHH is illustrated in Figure 5.6 for the 24th of July 2020 at 12:00 UTC for the simulation of Matimba. For this, the wind speeds at the source were used in the cross-sectional flux method. Subplot (a) depicts the simulated NO_2 columns, the detected plume as well as the fitted curve and the polygons. Subplot (b) shows the Gaussian curve fits for the first four and last two polygons where both CO_2 and NO_2 were used for the curve fitting. Subplot (c) displays the estimated NO_2 and NO_x fluxes along the plume with their fitted exponential decays as dotted lines. For NO_2, the flux increases after the emission and peaks between 25 and 30 km. Conversely, the NO_x flux culminates in the first polygon between 0 and 5 km and decreases afterwards. With the new algorithm, the estimated NO_x emissions are 62.0 ± 13.0 kt/yr which is close to the true emissions of 78.6 kt/yr shown as the black dashed line. Using the old algorithm, the estimated NO_x emissions would only be 29.4 ± 6.2 kt/yr. In addition, the estimated NO_x decay time using the new algorithm is more realistic at 6.5 ± 1.4 h compared to the estimated 25.2 ± 5.3 h using the old algorithm.
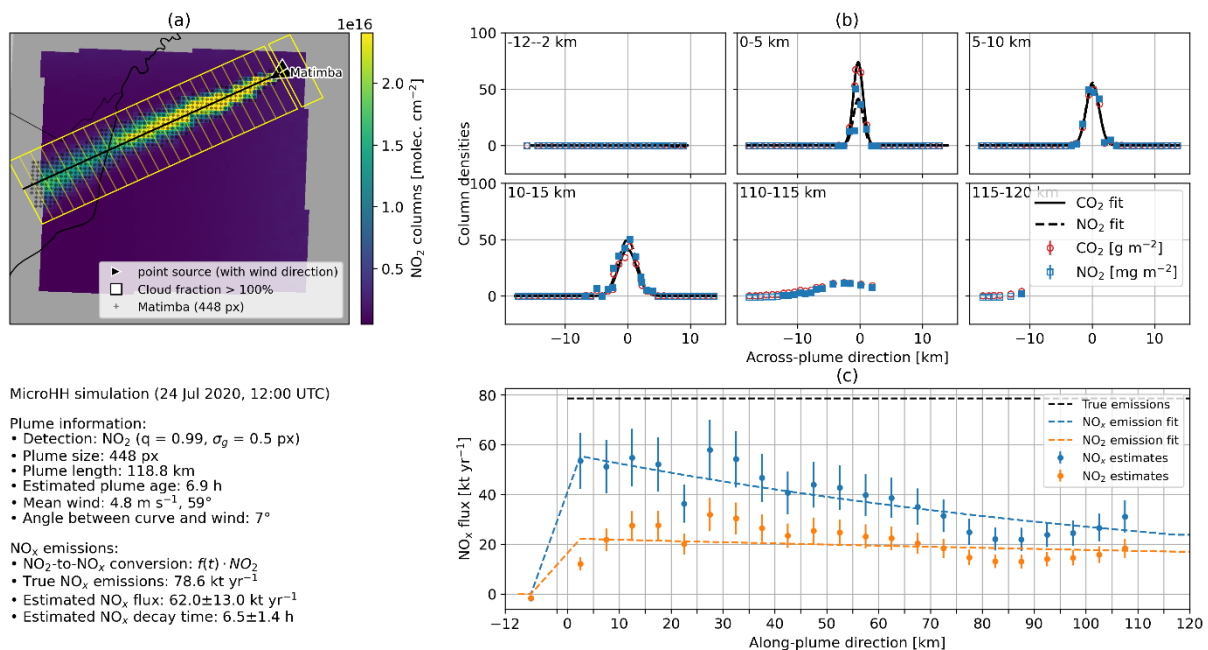
Figure 5.6: Overview of the application of the new algorithm to estimate NO_x emissions for the 24th of July 2020 at 12:00 UTC using the Matimba MicroHH simulation.

Figure 5.7 depicts the comparison of NO_x emission estimates for the MicroHH daytime time steps using the old and new algorithms and the wind speeds at the source. The results from the new algorithm are more in line with the estimates from the modelled NO_x fields and are in better agreement with the prescribed emissions. The median and standard deviation of the estimates are slightly higher for the new algorithm compared to that of the modelled NO_x fields.
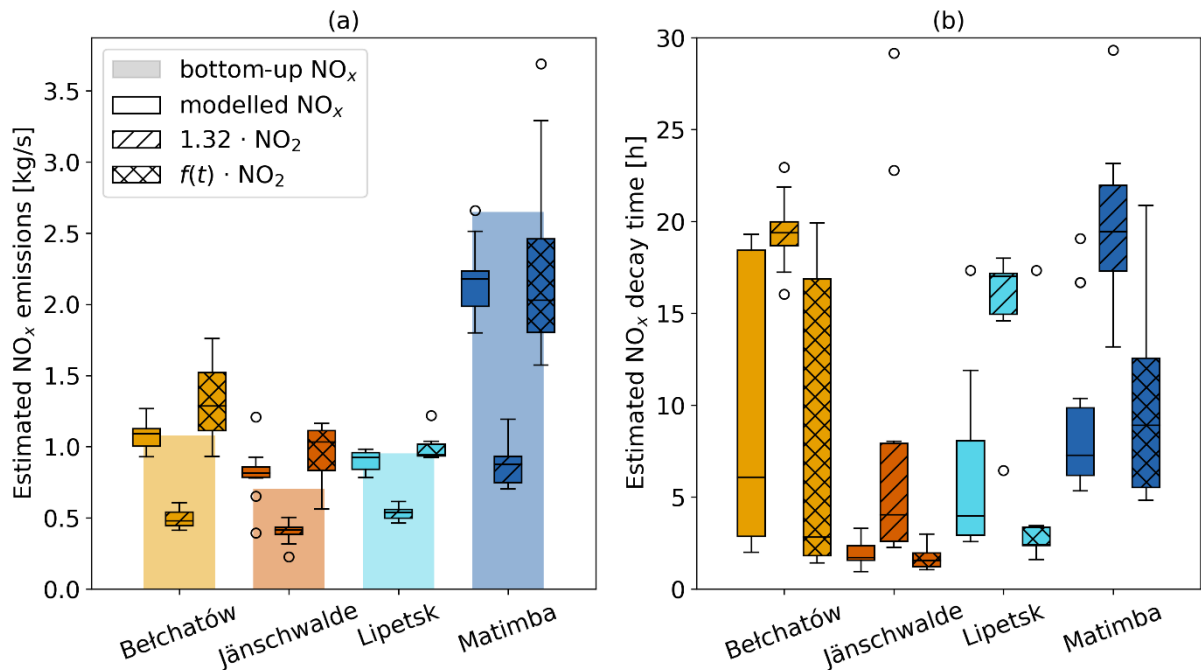
Figure 5.7: (a) Comparison of estimated NO_x emissions against the bottom-up reported and (b) estimated NO_x decay times using the old and new algorithms as well as the modelled NO_x fields. Only the daytime time steps of the MicroHH simulations were utilised and for the wind speed, the source wind was used.

Similar to the estimated emissions, the estimated NO_x decay times using the new algorithm are more consistent with those from the modelled NO_x fields. The median decay times are between 1.7 and 8.9 h whereas the estimates for all four cases using the old algorithm are more than twice as high.

With regard to the mean bias error of the estimated NO_x emissions of the daytime time steps, the new algorithm produces biases that are more consistent with those of the modelled NO_x fields. Nevertheless, the bias is slightly higher with the new algorithm compared to the modelled NO_x fields for all cases.

Using the backward integrated winds instead of the source wind for the same analysis as above slightly reduces the variability of NO_x emission estimates but significantly increases the variability of the NO_x lifetimes for the modelled NO_x fields and the new algorithm (see Figure A.2). However, the median lifetimes are comparable to those in Figure 5.7 except for Matimba.

5.6 Calculation of the updated air mass factors

As described in section 4.7, the AMF is calculated based on the vertical NO_2 profiles of the TM5-MP model. Figure 5.8a shows such a TM5-MP profile for the TROPOMI pixel at the location of the Matimba power plant on the 25th of July 2020 at 12:00 UTC in dark blue. In addition, the individual MicroHH profiles for the extent of this pixel are plotted in grey as well as their mean in light blue. It can be seen that the NO_2 concentrations are enhanced by two orders of magnitude compared to the background concentrations of $3 \cdot 10^{-10}$ mol/mol within the PBL. This enhancement is not captured by the coarse resolution TM5-MP model profile. Figure 5.8b shows the distribution of AMFs when the NO_2 profile of the Matimba source pixel is replaced by each of the MicroHH profiles. Profiles with high concentrations within the PBL result in lower AMFs and vice versa. For example, the range of AMFs between 0.5 and 1 is caused by NO_2 concentrations higher than $5 \cdot 10^{-9}$ mol/mol. On the other hand, NO_2 concentrations between $5 \cdot 10^{-9}$ mol/mol and the background concentration lead to AMFs between 1 and 1.3. Thus, these AMFs show a spread of 0.3 around the default AMF, which corresponds to an uncertainty of the AMF of 25%. The large peak at 1.37 is caused by the MicroHH background concentration which is lower than the modelled NO_2 concentration in TM5-MP.
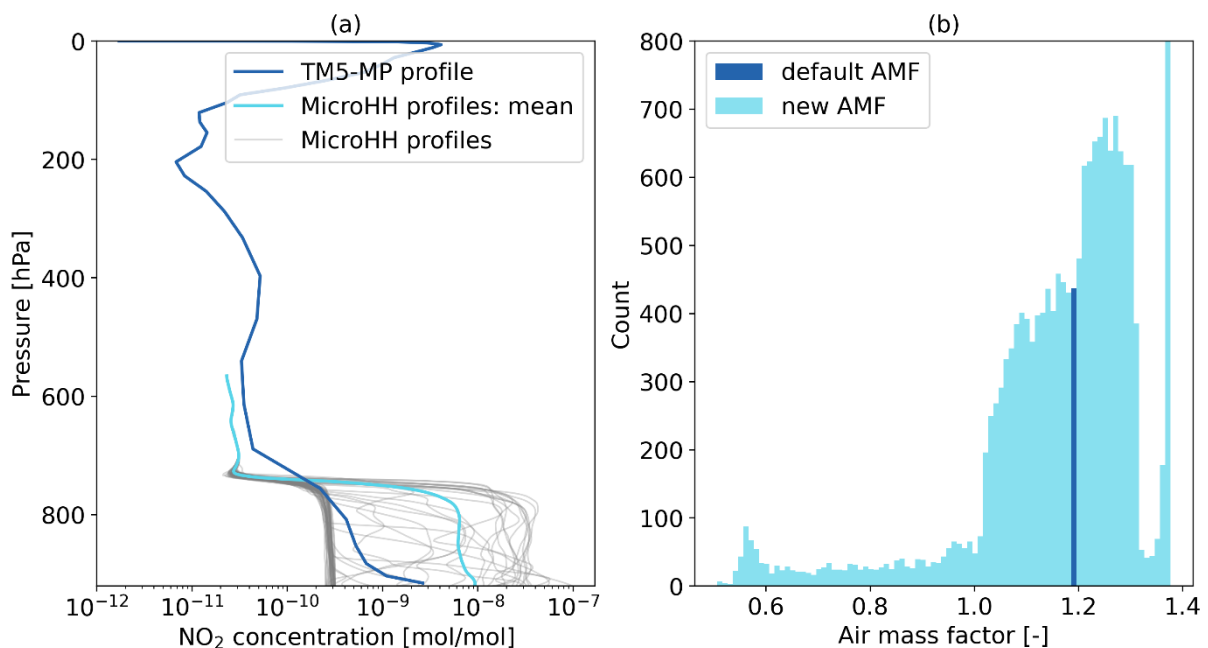
Figure 5.8: (a) TM5-MP and MicroHH NO_2 profiles of the Sentinel-5P source pixel for Matimba on the 25th of July 2020 at 12:00 UTC. (b) Histogram of the default and recalculated AMFs of the TROPOMI pixel containing Matimba power plant based on MicroHH NO_2 profiles.

Setting the NO_2 profiles within the PBL to a more realistic value of $5 \cdot 10^{-9}$ mol/mol for all TROPOMI images of Bełchatów, Jänschwalde, Lipetsk, and Matimba leads to the changes in

the AMF shown in Figure 5.9. It reveals that recalculating the AMF leads to lower AMFs compared to the default ones. For all sources, the standard deviations of the AMFs are around 0.12.
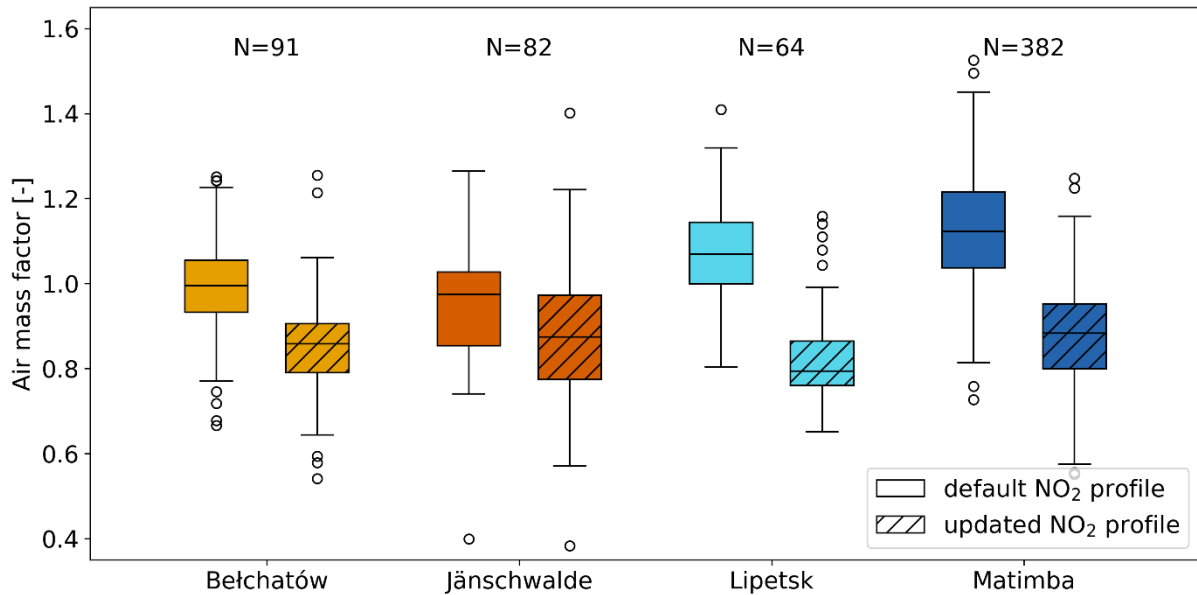
Figure 5.9: Default and updated AMF of TROPOMI images of Bełchatów, Jänschwalde, Lipetsk, and Matimba for the years 2020 and 2021. For the updated AMFs, the NO_2 concentration was set to $5 \cdot 10^{-9}$ mol/mol within the PBL of the detected plumes.

The relative differences between the old and new AMFs as well as the resulting increase in VCDs according to Eq. (4.9) are shown in Table 5.2.

Table 5.2: Relative change in AMFs and VCDs for NO_2 profiles set to $5 \cdot 10^{-9}$ mol/mol within the PBL for all TROPOMI images of Bełchatów, Jänschwalde, Lipetsk, and Matimba for the years 2020 and 2021.

Source	Relative difference in AMF	Resulting change in VCD
Bełchatów	-0.137	1.15
Jänschwalde	-0.102	1.11
Lipetsk	-0.159	1.35
Matimba	-0.214	1.27

Instead of setting the NO_2 profile of plume pixels to a predetermined value, it is also possible to iteratively approach the expected concentration. To this end, the relationship between the corrected NO_x mass and the median wind speed within the plume is quantified in Figure 5.10a. The corrected NO_x mass within the plume has a strong correlation with the median wind speed except for wind speeds below 4 m/s. Fitting Eq. (4.10) yields $a = 424$ and $b = $ -0.68 with a standard deviation $\sigma_a = 28.9$ and $\sigma_b = 0.038$. Applying this function to the median wind speed of each plume gives the estimated total NO_x mass in Figure 5.10b with a good correlation to the measured NO_x mass ($R^2 = 0.61$). The high spread of the NO_x mass at low wind speeds also leads to estimates which differ more from the measured values. Figure 5.10c shows the TM5-

MP NO$_2$ profile of the TROPOMI pixel containing the Matimba power plant (dark blue) and the updated NO$_x$ profile (light blue) with a concentration of $5.1 \cdot 10^{-9}$ mol/mol NO$_2$ in the PBL. In addition, all MicroHH profiles of the plume for the same time step are plotted (grey). It can be seen that the updated NO$_2$ profile represents the concentrations within the PBL much better than the TM5-MP profile. Using this profile to recalculate the AMFs leads to an increase of 30.6% which in turn results in VCDs that are 1.44 times higher than the default values.
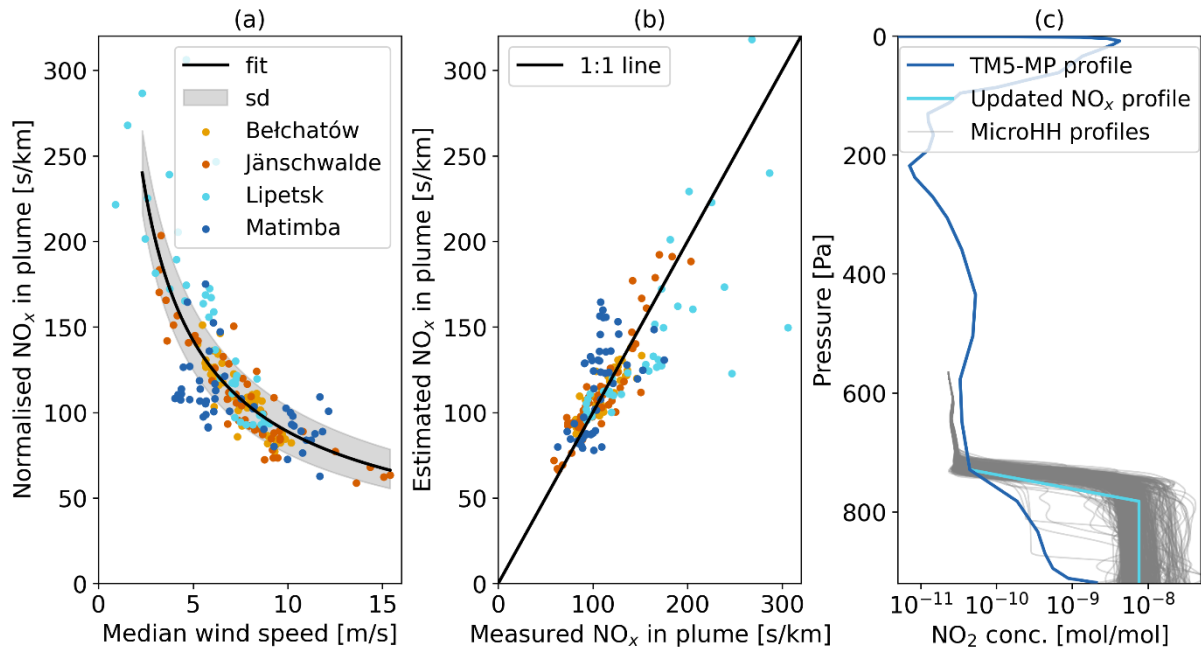
Figure 5.10: (a) Relationship between median wind speed and total NO$_x$ mass within the plume. (b) Measured and estimated NO$_x$ mass within the plume. (c) Updated NO$_2$ profile for the 25th of July 2020 at 12:00 UTC based on the estimated total NO$_x$ mass within the plume.

Ideally, the NO$_2$ profiles should be updated not only for the detected plume pixels but also for the background pixels. The exploratory approach, where the NO$_2$ concentration of the background pixels was set to $2 \cdot 10^{-10}$ mol/mol for the TROPOMI images of the 24th and 25th of July 2020 at 12:00 UTC resulted in an enhancement of the estimated NO$_x$ emission (see Figure A.3 and Figure A.4). For the 24th, they increased from 92.0 ± 15.7 kt NO$_x$ per year to 156.7 ± 26.8 kt, which is equivalent to an increase of 70.3%. For the 25th, only 57.1 ± 15.6 kt NO$_x$ per year were estimated for the default image, while the updated NO$_2$ profiles resulted in 81.1 ± 22.1 kt, which corresponds to an increase of 42.0%. These enhancements are much larger than the correction factor for Matimba calculated in Table 5.2.

5.7 Interpolation of bottom-up reported NO_x emissions

The comparison of the extrapolated expected CO_2 emissions for Bełchatów with those in Nassar et al. (2022) revealed that even if the annual CO_2 emissions and the hourly power generation were identical, the estimated hourly CO_2 emissions in the current study were 15% higher. Furthermore, if the emissions were correctly interpolated in both studies, there should be a linear relationship between power generation and NO_x emissions. However, this was not the case for some of the values in Nassar et al. (2022). For this reason, it is assumed that the emissions in the current study have been extrapolated correctly.

5.8 Application of the NO_2-to-NO_x conversion to TROPOMI

Table 5.3 lists the annual number of total TROPOMI images, the cloud-free images, those where the plume detection and centre line fit work, and the images that could be used to estimate emissions for the years 2020 and 2021.

Table 5.3: Annual number of TROPOMI images of Bełchatów, Jänschwalde, Lipetsk, and Matimba for the years 2020 and 2021 for different stages of the processing chain for NO_x emission estimation.

Source	Number of TROPOMI images per year			
	Total	**Cloud-free**	**Pl. det & c. fit**	**Est. emissions**
Bełchatów	737	64	36	32
Jänschwalde	807	42	17	9
Lipetsk	862	58	33	28
Matimba	454	206	171	153

At least two images per day were available for Bełchatów, Jänschwalde, and Lipetsk due to their high latitude. However, this had little positive effect on the number of usable images, because if one image was not usable due to high cloud cover, the following image from the same day could often not be used either. For these three sources, only about 7% of the total images were cloud-free, with plume detection working for half of them. For Matimba, almost half of the total available images were cloud-free, with plume detection working on more than 80% of these images.

Using *ddeq* to estimate the NO_x emissions from the TROPOMI data for the years 2020 and 2021 results in the estimated emissions shown in Table 5.4 and Figure 5.11. While the estimated emissions of the old algorithm reach between 40 and 60% of the bottom-up reported emissions, those derived with the new algorithm are more in line and reach about 65 to 90%. The AMF-corrected estimates are between 85 and 100% of the bottom-up emissions. For all four sources, these estimates are within one standard deviation of the bottom-up reported emissions. This is

also likely to be the case for Lipetsk where reported emissions from the steel and power plant are expected to be somewhere below 27 kt/yr (Guevara et al., 2023; NLMK Group, 2021).

Table 5.4: Median and standard deviation of estimated NO_x emissions in kt/yr for the years 2020 and 2021 for Bełchatów, Jänschwalde, Lipetsk, and Matimba derived from TROPOMI images.

Source	Median NO_x emissions [kt/yr]			
	$1.32 \cdot NO_2$	$f(t) \cdot NO_2$	$f(t) \cdot NO_2 \cdot C_{AMF}$	Bottom-up
Bełchatów	12.3 ± 2.9	19.4 ± 5.5	22.3 ± 6.4	25.1
Jänschwalde	7.1 ± 1.6	10.4 ± 2.0	11.5 ± 2.3	11.6
Lipetsk	12.8 ± 3.2	15.4 ± 4.7	20.8 ± 6.4	–
Matimba	40.8 ± 11.9	69.1 ± 29.8	87.8 ± 37.8	103.4

Similar to Figure 5.7, the range of estimated emissions in Figure 5.11a is largest for Matimba. This source also has the largest number of outliers. The relative mean bias error in Figure 5.11b is comparable for all four sources for a given method of estimating the NO_x emissions. While the bias is more than -50% relative to the bottom-up reported emissions with the old algorithm, it is reduced to -20 to -30% with the new algorithm and to only -12 to -20% with the AMF correction.
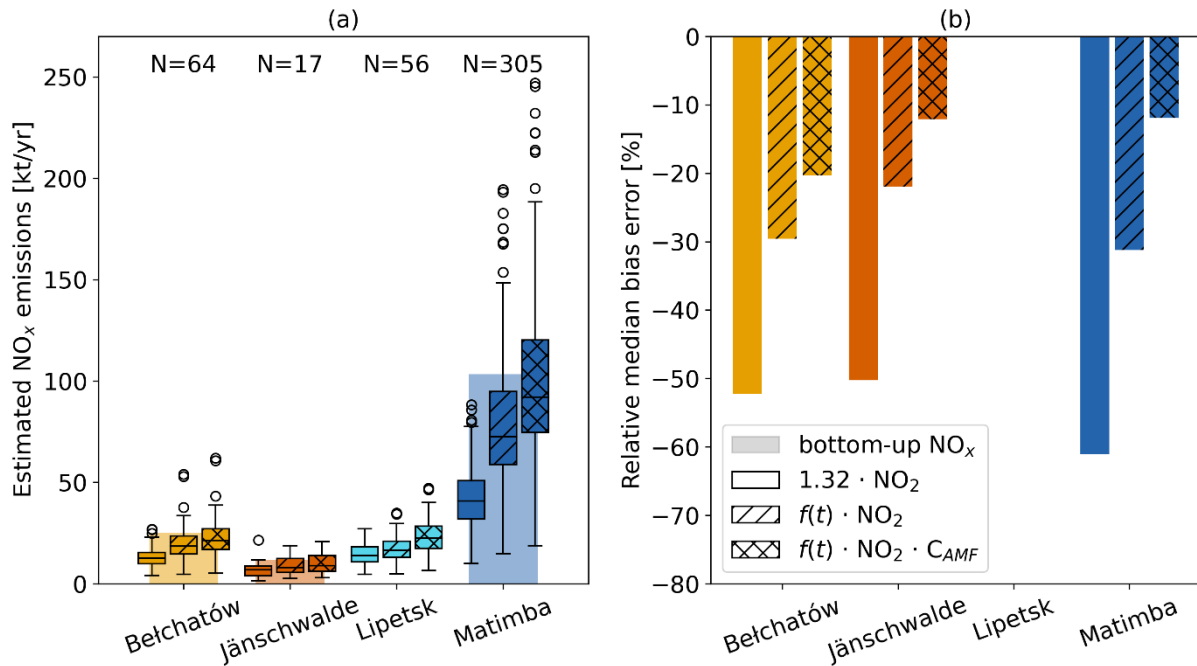
Figure 5.11: (a) Estimated NO_x emissions and (b) their relative median bias errors for Bełchatów, Jänschwalde, Lipetsk, and Matimba for TROPOMI data of the years 2020 and 2021.

The uncertainties of the single-overpass and annual estimates are listed in Table 5.5. The first column shows the median of all single-overpass estimate uncertainties. The second column represents the standard deviation of the difference between estimated and bottom-up reported emissions. These values are larger than those in the first column for two of the three cases. The

third column shows the uncertainties in annual emissions according to error propagation (see Figure A.6), while the fourth column includes uncertainties in diurnal and seasonal cycles.

Table 5.5: Uncertainties of NO_x emission estimates for single-overpass and annual estimates for Bełchatów, Jänschwalde, Lipetsk, and Matimba.

Source	Single-overpass estimates [%]		Annual estimates [%]	
	Median uncertainty	SD of bottom-up - est. NO_x	Spline uncertainty	Total uncertainty
Bełchatów	22.4	21.1	6.2	9.7
Jänschwalde	24.3	25.4	12.2	19.0
Lipetsk	19.8	–	6.8	10.5
Matimba	27.4	41.2	1.5	3.7

The sensitivity analysis of the NO_2-to-NO_x conversion factor shows that applying the factor for Jänschwalde to all four sources leads to emission estimates that are 15.7% lower for Bełchatów, 18.8% higher for Lipetsk and 22.9% lower for Matimba. Using the conversion factor of Matimba for all four sources results in 12.8% higher emissions for Bełchatów, 41.6% higher for Jänschwalde and 51.4% higher for Lipetsk.

6 Discussion

6.1 NO$_x$ chemistry in plumes

The main objective of this study was to develop a more realistic model for a conversion factor of NO$_2$ to NO$_x$ that accounts for NO$_x$ chemistry in plumes. Therefore, the results of the current study depend heavily on the correct simulation of the NO$_x$ chemistry in MicroHH. This in turn depends on several factors such as the chemistry scheme, model resolution and boundary conditions. Although MicroHH uses an existing chemistry scheme and established boundary conditions, it is difficult to estimate the accuracy of its chemistry due to the influence of model resolution. This is because the resolution determines small-scale structures in the dispersion of the trace gases, called eddies, which are caused by turbulence. The higher the resolution, the more eddies can be observed which create a larger surface area between the plume and the ambient air, where most of the reactions take place (see section 2.4) (Koene and Brunner, 2023).

The MicroHH simulations are currently the highest-resolution chemistry transport simulations applied at these scales. Consequently, no study has compared the modelled trace gases concentrations with observations yet. Such analyses exist only for the IFS chemistry scheme, on which the one implemented in MicroHH is based. For example, Flemming et al. (2015) showed that the IFS chemistry scheme can capture the dynamics of NO$_2$ concentrations measured by satellites and surface observations. The deviations found were attributed to the underestimation of prescribed NO emissions, NO$_2$ lifetimes, and the simplified simulation of NO$_x$ reservoir species (Flemming et al., 2015). A more recent study by Huijnen et al. (2022) using the same chemistry scheme also found good agreement between simulated and satellite derived NO$_2$ fields. However, especially over areas of high emissions, such a comparison suffers from the same biases due to the AMFs as seen in section 5.6.

As an in-depth analysis of the accuracy of the NO$_x$ chemistry in MicroHH is beyond the scope of this analysis, it is assumed to be realistic enough for the purpose of this study. The assumption is supported by the fact that the MicroHH simulations have an unprecedented resolution and that their chemistry scheme is tuned to the well-established NO$_x$ chemistry of the IFS.

The understanding of the NO$_x$ chemistry in plumes has mainly been achieved by analysing the NO$_x$:NO$_2$ ratios in plumes. As seen in section 5.1, the ratios are much higher near the source because most of the NO$_x$ is emitted as NO which is then oxidised to NO$_2$. The ratio is also higher at night because O$_3$ is titrated and none is produced due to the absence of photolysis. As a result, a higher proportion of NO remains, leading to a higher NO$_x$:NO$_2$ ratio (see section 2.4).

A higher NO_x:NO_2 ratio can also be seen in Figure 5.4 for the Matimba case compared to the other three simulations. The main reason for this that the Matimba simulation was run on the 24th and 25th of July, which is during the southern hemisphere winter. Accordingly, the SZA is larger than for the other three cases, resulting in lower irradiances and photolysis rates. Another reason in the higher NO_x:NO_2 ratios could be the lower background concentrations of O_3 and VOCs for Matimba (see Figure A.1), which is due to the lower proportion of land mass in the southern hemisphere with smaller anthropogenic sources of NO_x and VOCs. As a result, the HO_x/NO_x cycle is slower and less O_3 is produced (see section 2.4) (Seinfeld and Pandis, 2006). In addition, the lower temperatures in winter lead to slower reaction rates (Seinfeld and Pandis, 2006). It is also likely that the NO_x:NO_2 ratio is influenced by the amount of NO_x emitted: the more that is emitted, the longer it takes for the plume to mix sufficiently to reach the photo-stationary state. This may be one of the reasons why the NO_x:NO_2 ratio for Bełchatów levels off at a higher value for f_0 compared to Jänschwalde and Lipetsk, even though they are at similar latitudes and have similar background concentrations of NO_x, O_3, and VOCs (see Figure A.1).

The explanations for higher NO_x:NO_2 ratios outlined above can also be found in the importance of the explanatory variables in the RF implemented exploratively in this study. As seen in section 5.4, the most important factor determining the intercept m is the photolysis rate, as it governs the amount of O_3 available for the oxidation of NO to NO_2. On the other hand, the temperature controls the variable τ the most, as it determines the rate of the O_3 producing reactions. Finally, photolysis rates and prescribed emissions appear to have the greatest influence on the offset value f_0, as the former determines how much of the NO is oxidised to NO_2, while the latter determines the quantity of NO available for oxidation. For all three parameters, the background concentration of CO is also important as its reaction with OH radicals can initiate a chain of reactions leading to the oxidation of NO by HO_2 (Seinfeld and Pandis, 2006).

To summarise, the different NO_x:NO_2 ratios in the four MicroHH simulations are the result of different photolysis rates, temperatures, trace gas background concentrations and emitted quantities. A RF regression could realistically determine these factors.

6.2 Conversion of NO_2 to NO_x in plumes

Ideally, the factors controlling NO_x chemistry would be considered to determine the conversion of NO_2 to NO_x. This could be achieved using machine learning as the effects of photolysis rates,

temperatures, and trace gas background concentrations on NO_x chemistry are expected to be non-linear. However, using the RF tested in this study to convert NO_2 to NO_x resulted in higher variances in the NO_x emission estimates compared to the negative exponential functions in section 5.4. One reason for this could be that the RF was trained using all 48 time steps of the MicroHH simulations while the negative exponential functions were fitted using only the daytime values. Consequently, these functions could be overfitted when estimating NO_x emissions of the same time steps.

Overall, the implemented RF shows the potential of machine learning to convert NO_2 to NO_x. For this purpose, a more sophisticated model, such as a convolutional neural network, could be applied. Once trained, it could predict the NO_2-to-NO_x conversion factors without the need to run a high-resolution chemistry transport model for each plume. However, a number of such models covering a wide range of conditions would need to be run for proper training and validation of a machine learning model. Alternatively, Kuhlmann et al. (2021) suggested a look-up table of NO_2-to-NO_x conversion factors that could be obtained from chemistry transport simulations. As both approaches were beyond the scope of this study, the four fitted negative exponential functions in Table 5.1 were used to convert NO_2 line densities to NO_x.

Applying these conversion factors to the MicroHH data as a validation shows that they can well account for the NO_x chemistry: While the amount of NO_2 in Figure 5.6 increases after emission due to the oxidation of NO to NO_2, the NO_x line densities are highest at the source as expected. Consequently, section 5.5 shows that the NO_x emission estimates with the new algorithm are in good agreement with the NO_x estimates from the modelled NO_x fields. The same applies to the NO_x lifetimes, which are more than halved with the new algorithm. This is because the NO_2 fluxes are converted to NO_x by multiplication with a negative exponential function. As a result, the exponential decay fitted to the NO_x fluxes to determine their lifetimes is steeper, leading to shorter lifetimes (see section 2.7). Therefore, the lifetimes are closer to the four hours derived in previous studies (e.g., Beirle et al., 2011), which was calculated for Riyadh. As photolysis rates are higher in Riyadh compared to e.g., Matimba in winter, the lifetimes are higher for the latter. The largest discrepancies between the estimated NO_x emissions from the modelled NO_x fields and the new algorithm for Bełchatów and Jänschwalde are probably due to the higher uncertainties of the fitted negative exponential functions. Nevertheless, the estimated emissions and lifetimes are a significant improvement over the previous approach of converting NO_2 to NO_x using a constant factor of 1.32.

The aim of the new algorithm is to achieve good agreement between the NO_x emission estimates using the modelled NO_x fields and those using the new algorithm. This implies that the new algorithm fully captures the NO_x chemistry – assuming a realistic representation of the NO_x chemistry in MicroHH. The remaining discrepancy between estimated and prescribed emissions is therefore due to biases in the cross-sectional flux method. One such source of biases is the wind speed used to convert line densities to fluxes, which will be discussed in section 6.4. The biases of the new algorithm are more in line with those of the modelled NO_x fields but are slightly larger because the implemented conversion of NO_2 to NO_x does not take into account the specific meteorological and background conditions of each time step, but the median conditions. Thus, the bias is likely to increase when the NO_2-to-NO_x conversion factors derived in this study are applied to annual data, as the conditions under which these conversion factors were derived do not match those in the annual data.

Nevertheless, these four fitted NO_2-to-NO_x conversion factors can be applied to annual TROPOMI images for two reasons. First, most of the images that can be used for plume detection were acquired between April and October (see Figure A.5). Images taken during the rest of the year often cannot be used for NO_x estimation due to high cloud cover. Consequently, the prevailing conditions for most of the emission estimates are comparable to those in the MicroHH model runs, which simulated days in May to July (see Table 3.1). Second, the four NO_2-to-NO_x conversion factors cover both winter and summer cases as well as different background conditions such as maritime for Matimba and continental for the other three. Conducting a sensitivity analysis by using the NO_2-to-NO_x conversion factors of Jänschwalde (summer case) and Matimba (winter case) to estimate NO_x emissions of all four sources therefore provides a possible range of NO_x emission estimates.

In conclusion, the newly implemented conversion factors for NO_2 to NO_x have shown a significant improvement in the estimation of NO_x emissions from MicroHH simulations and are therefore considered suitable for the application to TROPOMI images.

6.3 Quantification of NO_x emissions from TROPOMI

The application of the new NO_2-to-NO_x conversion to the TROPOMI data in section 5.8 has shown that the NO_x emission estimates obtained with the new algorithm are much closer to the bottom-up reported emissions than the estimates from the old algorithm with a constant NO_2-to-NO_x conversion factor of 1.32. Correspondingly, the relative median bias has decreased from

more than -60% to -12%, especially after applying the AMF correction factor. However, as mentioned in section 5.6, the emission estimates increase even further if the AMFs are updated not only for the detected plume, but also outside the plume (see also section 6.5). This leads to an even better agreement between bottom-up reported and estimated emissions or possibly an overestimation which would be in line with the overestimation of NO_x emissions when using the new algorithm in Figure 5.7. The reason for such an overestimation could be that the NO_2-to-NO_x conversion factors were fitted using all simulated daytime time steps from MicroHH and not only the ones at TROPOMI overpass. Furthermore, the implemented NO_2-to-NO_x conversion cannot not take into account the specific meteorological and background conditions of individual TROPOMI images. Thus, the fitted parameters in Table 5.1 might be too high.

It is worth noting that the range of NO_x emission estimates for Matimba is the widest for both MicroHH and TROPOMI data. The most likely explanation is that the plumes are the longest for Matimba. Therefore, parts of the plume are several hours old and have been subject to different chemistry and wind speeds. This results in outliers in the NO_x fluxes along the plume, leading to mismatched emission fits. The fact that the variance of the estimated emissions for MicroHH decreased slightly when using the backward integrated winds in section 5.5 indicates that this procedure can partially account for the temporal changes in wind speeds. However, the simplicity of backward integration limits its impact, which will be discussed in section 6.4. In addition, it cannot account for temporal changes in chemistry.

As the number of successful emission estimates per year has a large influence on the uncertainties of the annual emission estimates, maximising the number of suitable satellite images is crucial. Nevertheless, only a fraction of the TROPOMI images could be used for Bełchatów, Jänschwalde, and Lipetsk due to cloud cover (see Table 5.3). Especially between October and February, emissions could only be estimated for a few days (see Figure A.5). The strong seasonal bias in the number of successful estimates may lead to an underestimation of annual emissions as most emissions are expected to occur in winter due to the higher electricity demand. This gap cannot be filled by the upcoming Sentinel-5 satellite either but could be alleviated by existing and upcoming geostationary satellites such as GEMS, TEMPO, and Sentinel-4: The hourly temporal resolution increases the probability of obtaining a usable image on a cloudy day (EoPortal, 2023, 2014). It would also allow to resolve the diurnal cycle of NO_x emissions, which currently cannot be captured with only one or two overpasses around noon. However, GEMS, Sentinel-4, and -5 have a coarser resolution than Sentinel-5P (EoPortal, 2014, 2013).

The problems caused by a coarse spatial resolution can be seen in the example of Jänschwalde in Table 5.3: As there are two coal-fired power plants in the vicinity of Jänschwalde, the plumes often mix, which is why the emissions cannot be estimated using the cross-sectional flux method (see section 2.6). This also applies to Bełchatów, but to a lesser extent. In contrast, fewer sources are located around Lipetsk and Matimba which could lead to overlapping plumes. As shown in Kuhlmann et al. (2021), a satellite with higher spatial resolution, such as CO2M, can help to better differentiate between plumes, mitigating the challenge of overlapping plumes.

The comparison of the uncertainties of the NO_x emission estimates in this study with those in Kuhlmann et al. (2021) highlights the importance of the number of successful emission estimates. The uncertainties of the annual emissions between 3.7 and 19% in this study are significantly lower than the uncertainties of 16 to 73% and 13 to 52% for two and three of the CO2M satellites in Kuhlmann et al. (2021). The reasons are the higher temporal resolution of TROPOMI compared to CO2M and the high source strength of the power plants considered in the current study. A comparison of the uncertainties of the single-overpass estimates due to random error between the two studies reveals that those in the current study are marginally lower than the 29% derived in Kuhlmann et al. (2021). This difference may be attributed to the consideration of additional uncertainties in their study by including a source strength dependent factor and an offset. The uncertainties of single-overpass estimates in Table 5.5 would agree with those in the second column if the bottom-up reported emissions corresponded to the true emissions and all uncertainties were included in the emission estimation. However, the larger magnitude of the values in the second column indicates the presence of other uncertainties which were not considered in the emission estimation. These include the simplified representation of instrument noise, wind speed, and AMFs. On top of these random errors, there are uncertainties due to systematic errors such as the representation of wind speeds, the estimation of background concentrations, the application of the NO_2-to-NO_x conversion factors to annual data, and methodological uncertainties, which are not represented in the estimated uncertainties.

The systematic biases due to the application of the NO_2-to-NO_x conversion factors to annual TROPOMI data were investigated in the form of a sensitivity analysis in section 5.8: Applying the NO_2-to-NO_x conversion factors of Jänschwalde and Matimba to all four sources resulted in emission estimates ranging from 10% lower to 50% higher, which illustrates that the parametrisation of the NO_2-to-NO_x conversion adds a significant but unknown uncertainty to the emission estimates. This is because it is not possible to determine how well the conditions under which these parametrisations were derived match those of a given TROPOMI image. Still, the

deviations of the sensitivity analysis from the estimated NO_x emissions with the source specific parameters give a maximum range of uncertainties. Since most of the suitable satellite images are from the season for which the MicroHH simulations were run, the calculated NO_2-to-NO_x conversion factors are likely to be in good agreement with the conditions of the TROPOMI images. However, in order to get a better understanding of the uncertainties, it would be necessary to run more high-resolution chemistry transport simulations covering a wider range of conditions. The sensitivity analysis thus shows a limitation of the current approach to convert NO_2 to NO_x.

Another limitation is the choice of the negative exponential function in Eq. (4.5). While this function may be appropriate for point sources such as power plants, it may not be suited for cities where emissions occur over several kilometres in the direction of the plume (Lorente et al., 2019). Instead of a negative exponential function, a log-normal or gamma distribution should be fitted which accounts for the build-up of NO_x over the city.

Overall, the application of the newly developed NO_2-to-NO_x conversion factors resulted in more accurate emission estimates compared to the previous constant conversion factor of 1.32. These results therefore support the working hypothesis that NO_x and consequently CO_2 emissions can be estimated more accurately from NO_2 observations. Nevertheless, extrapolating the conversion factors for different meteorological and background conditions remains a challenge.

6.4   Effective wind speeds in plumes

Apart from the NO_x chemistry, a realistic representation of the effective wind speed at which the plume is transported is a key issue. This includes the vertical averaging of 3D wind fields and the consideration of time-varying wind fields. To address the first challenge, the 3D wind speeds were weighted with the GNFR-A profile (e.g., Figure 5.2a). An advantage of this method is that the derived winds are representative even in cases where the PBL is below the height of the stacks. However, this is usually not the case at the Sentinel-5P overpass time at 13:30 local time when the boundary layer is well developed. Nevertheless, it becomes relevant for the backward integration of the wind. Using the GNFR-A profile-weighted winds has the added advantage of corresponding better to the plume when it is not well mixed within the PBL. This is the case for stable atmospheric conditions and close to the source. On the other hand, with increasing distance from the source, the trace gases become progressively well mixed within the PBL. Depending on meteorological conditions, a homogenous mixing can occur within the

first few kilometres of the plume (Honnert et al., 2021; Koene and Brunner, 2023). Consequently, the approach of using the mean wind speed within the PBL is more appropriate in these situations. However, this approach should only be used up to a certain minimum PBL height, below which the flue gases are emitted into the free troposphere. For some power plants, this may occur if the PBL height is below the stack height or if the flue gases overcome the PBL due to buoyancy. Such a situation could arise in winter and, in combination with the backward integrated winds, in the morning when the PBL is shallow. For the PBL-weighted wind speeds, the threshold was set to mode of the GNFR-A profile at 400 m. Conversely, Brunner et al. (2019) have shown for Jänschwalde that the plumes rise on average only to about 250 m height in winter, but up to 360 m in summer. They are strongly influenced by the dynamics of the PBL, which has a distinct diurnal cycle, especially in summer. These results suggest that a fixed cut-off at 400 m, as it is implemented for the current averaging of the PBL winds, is too conservative. As mentioned in section 4.2, this threshold should be dynamic and account for parameters such as stack height, flue gas properties, and meteorological conditions (Brunner et al., 2019). On the bottom line, the two approaches for vertically averaging the 3D wind fields excel in different situations. Nevertheless, further studies are needed to assess the suitability for different conditions or to examine a combination of both methods.

To meet the challenge of temporally changing wind fields, a backward integration of wind speeds is required: The analysis of ERA5 wind speed data with its spatial resolution of $0.25° \times 0.25°$ has shown that the wind fields exhibit little variation in space because the effects of turbulence are averaged out. However, the wind speeds show large variations in time. This is particularly the case for the lower troposphere, where the evolution of the PBL has a crucial influence on the wind, as wind speeds in the free troposphere are typically higher than those within the PBL. As parts of the plume were emitted hours prior to the overpass of the satellite, the trace gases were transported at different wind speeds than the prevailing wind at the time the image was taken, which violates the steady-state assumption of the cross-sectional flux method (see section 2.6). Thus, integrating wind speeds backwards in time should make it more realistic. According to the conservation of mass, a higher wind speed at a constant emission rate would lead to a lower trace gas line density and vice versa. Therefore, a negative correlation between wind speed and line density is expected. Consequently, if the backward integration of the wind works as intended, the correlation should be stronger than if the wind speed at the source is used. This is also the case in Figure 5.3, indicating a slight improvement over using only the wind speed at the source at the time of the satellite overpass. Nevertheless, the analysis of the backward integrated wind has shown that the wind direction does not always correspond

to the direction of plume propagation. This was observed for both the GNFR-A weighted wind and the mean PBL wind, showing that the backward integration approach used in this study is too simple.

A further limitation of the backward integration of the wind was revealed in section 5.5, where the use of backward integrated wind speeds significantly increased the variance in NO_x lifetimes. This occurs because the GNFR-A profile includes winds up to 1000 m. When the PBL is below this threshold, e.g., in the morning, the vertically averaged wind speeds also include the higher wind speeds of the free troposphere, resulting in higher vertical averages. As the tail of a plume is sometimes several hours old, its line densities are multiplied by higher wind speeds than close to the source, leading to higher fluxes. As a consequence, the fitted NO_x decay is less steep, yielding longer lifetimes.

To address the inaccuracies of the backward integrated wind, 3D transport models would have to be run, contradicting the aim of a computationally light method such as the cross-sectional flux method. Another approach could be to assign uncertainties to the wind speeds which are inversely proportional to the distance from the source, thereby accounting for the additional uncertainties and allowing for a more stable fit of the exponential NO_x decay along the plume. Another possibility would be to omit the information from polygons beyond a certain distance from the source. The motivation for this cut-off is threefold: First, the uncertainty of the backward integrated wind increases for longer plumes. Second, it is almost impossible to determine the effective wind speed at which the plume was transported at a time when the flue gases are partly emitted into the PBL and partly into the free troposphere. Third, the tail of long plumes was subject to different atmospheric conditions and chemistry, as it was emitted several hours before the satellite image was taken, violating the assumption of steady-state conditions. Such a cut-off was implemented exploratively for the PBL averaged winds (see section 4.2). The analysis of a few time steps showed that the median of the estimated NO_x emissions was similar to the estimates obtained when using the full plume information, while outliers were reduced. Thus, considering only plume information up to a certain plume length or time since emission appears to be reasonable.

Besides the challenges of the vertical averaging of 3D wind fields and the consideration of time-varying wind fields, further investigation is needed to revise the simplified assumption of a constant wind speed uncertainty of 1 m/s. This value is significantly higher than the calculated systematic uncertainty of ERA5 wind speeds in Gualtieri (2022), because it should also take into account uncertainties of the vertical averaging of the 3D wind fields. However, the

accuracy of this assumption is unknown. Therefore, numerical transport simulations would have to be run to determine the deviations between the vertically averaged wind speed and the effective wind speed of the plume. These uncertainties could then be combined with the ensemble spread of ERA5 and the deviations of ERA5 from observations to obtain an overall wind speed uncertainty.

6.5   Impact of air mass factors

The TM5-MP model used to calculate the TROPOMI AMFs cannot resolve individual plumes due to its coarse resolution of $1° \times 1°$. Thus, the NO_2 fields in TM5-MP do not have spatially confined plumes with elevated concentrations, but concentration gradients. As a result, the modelled pixels have neither the correct concentration profile of the plume nor the background concentration, but a mixture of both. This leads to an overestimation of AMFs and a consequent underestimation of VCDs within the observed plumes and vice versa outside of the plumes. The impact of this effect was explored in section 5.6 of the current study by replacing the NO_2 profiles of pixels within the plume with higher concentrations, while replacing the profiles of pixels outside the plume with a representative background concentration. This approach resulted in the expected enhancement of plume VCDs, while the background VCDs were reduced. As the NO_2 background concentrations are subtracted from the plume enhancements, updating the AMF within and outside the plume increases the estimated emissions more than if solely the profiles within the plume were updated. Accordingly, the estimated emissions for the two TROPOMI images of Matimba increased by 70% and 42% compared to the default NO_2 profiles. Such an enhancement is significantly higher than the 27% increase shown in Table 5.2. These results illustrate that the a-priori NO_2 profiles of the TM5-MP model should ideally be replaced by profiles from higher resolution models such as GEM-MACH (Goldberg et al., 2019b) or CAMS-regional (Douros et al., 2023). However, updating the AMFs for all pixels was beyond the scope of this study.

Instead, the estimated NO_x emissions were multiplied by correction factors derived from updating the NO_2 profiles within the plume for all TROPOMI images (see Table 5.2). Such an approach is sufficiently accurate because the analysis of the MicroHH plumes showed that the average NO_2 concentration within the PBL in the four modelled plumes was consistent at $5 \cdot 10^{-9}$ mol/mol. Setting the NO_2 to this concentration resulted in correction factors between 1.15 and 1.35 while other studies have calculated significantly higher corrections. For example, Beirle et al. (2019) found that VCDs need to be corrected by a factor of 1.35 for South Africa

and 1.98 for Germany. The higher values are due to the assumption of Beirle et al. (2019) that the entire plume is confined between 60 and 200 m above ground where the averaging kernel are typically smaller than at higher altitudes (see section 2.5). In contrast, the correction factors in this study were calculated assuming a homogeneous distribution in the PBL, which is more realistic except for stable atmospheric conditions. Douros et al. (2023) analysed the impact of replacing the TROPOMI a-priori NO_2 profiles over Europe with data from the higher resolution CAMS-regional model at a resolution of $0.1 \times 0.1°$. They found that the NO_2 VCD increased by a factor of 1.05 for less polluted sites and up to 1.3 for more polluted sites. These values are in perfect agreement with those in Table 5.2, which illustrates that the AMF correction factors derived in this study are realistic.

Replacing the NO_2 profiles within the PBL by a constant concentration is too simplistic as it depends on, among other things, the emission strength of the source. For this reason, a simple iterative approach to determine a representative NO_2 concentration within the PBL was presented in section 4.7. The results in Figure 5.10c showed that the derived profile is very similar to the plume profiles in the MicroHH simulations, illustrating the potential of this approach. However, one limitation of this method is that, while the total NO_x mass can be reliably estimated, its uniform distribution across the polygons of the plume leads to poorer agreement between the measured and estimated NO_x mass. This issue arises because such a uniform distribution neglects the effects of NO_x chemistry. Therefore, the proposed method could be improved by assigning the NO_x mass along the plume according to a negative exponential function, as in Eq. (4.5).

Besides the underestimated NO_2 profiles in plumes discussed above, there is an additional uncertainty in the AMFs because the exact NO_2 profile is not known. In this study, these uncertainties were not systematically investigated, but in an exploratory approach. In doing so, the 25% uncertainty derived for an example of Matimba in section 5.6 is consistent with the 30% uncertainty reported in Beirle et al. (2019). However, a thorough assessment of the uncertainties introduced by the AMF is required.

Overall, the results have shown that the systematic bias in the AMFs could be realistically corrected for in the current study. Furthermore, the iterative approach to update the NO_2 profiles in the plumes yielded promising results but needs further refinement.

6.6 Bottom-up reported emissions

Knowledge of bottom-up reported NO_x and CO_2 emissions is important in this study for two reasons. First, they are used to assess the accuracy of the estimated NO_x emissions from satellites. Second, they can be used to convert the estimated NO_x emissions into CO_2 (see section 2.3). For both applications it is crucial to have information on the reliability and accuracy of the bottom-up reported emissions. However, many of the bottom-up reported CO_2 emissions are estimated from fuel consumption, making assumptions about combustion efficiency, fuel purity and other factors (IPCC, 2006). The use of proxies to estimate emissions not only introduces many uncertainties, but also leads to gaps between reported emissions and inventories (Guan et al., 2012). Similarly, the uncertainties are not measured directly, but estimated from the intercomparison of different data bases (e.g., Guan et al., 2012; Gurney et al., 2016), from statistical methods (e.g., Zhao et al., 2011), or from proxies such as fuel consumption and electricity generation (e.g., Guevara et al., 2023b [preprint]). For example, Nassar et al. (2022) assumed a 5% uncertainty in reported CO_2 emissions for Bełchatów, arguing that, due to its large size, it is at the lower end of the estimated uncertainties from a paper by Gurney et al. (2016). For NO_x, Zhao et al. (2011) estimated the uncertainties in reported emissions from coal-fired power plants in China to be around 17%, illustrating the inaccuracies in reported emissions. However, it is not known whether the assumptions used to estimate or interpolate emissions from proxies are valid as there are currently no studies at the power plant level. For example, power plants may operate in different modes, resulting in different emissions for comparable power output.

In summary, the knowledge on the accuracy of bottom-up reported emissions and their uncertainties is limited, which requires further investigation. This is also the reason why no statistical test was performed to assess whether the estimated emissions from the new algorithm are more consistent with the bottom-up reported emissions than the estimates from the old algorithm.

Having little knowledge of the uncertainties in the bottom-up reported CO_2 and NO_x emissions also translates into uncertainties in the $CO_2:NO_x$ ratios. As these are used to convert estimated NO_x emissions into CO_2, the uncertainty of the estimated emissions is increased. The issue is further complicated by the fact that the $CO_2:NO_x$ ratio of one power plant cannot be easily applied to multiple power plants or extrapolated to different years because they have different NO_x abatement technologies which change over time due to stricter air quality regulations (Goldberg et al., 2019a; Liu et al., 2020; Reuter et al., 2014). Furthermore, obtaining accurate

CO_2:NO_x ratios is particularly challenging for mixed sources, such as in the case of Lipetsk, where emissions originate from industrial activities and a power plant.

To overcome the problem of inaccurate bottom-up reported CO_2:NO_x ratios, several case studies have explored the possibility of estimating them using satellites (e.g., Hakkarainen et al., 2021; Kuhlmann et al., 2021; Reuter et al., 2019). However, Kuhlmann et al. (2021) have demonstrated that with the upcoming CO2M satellites, which measure CO_2 and NO_2 simultaneously, the uncertainty of the estimated CO_2 emissions is smaller when using bottom-up reported CO_2:NO_x ratios if these are well known. This was due to large uncertainties in the estimated NO_x emissions resulting from a simplified representation of NO_x chemistry. As this aspect has been improved with the current study, the use of satellite-derived CO_2:NO_x ratios has become a viable method to convert NO_x into CO_2 emission estimates. Until the launch of CO2M, co-located observations from spaceborne CO_2 measuring instruments such as the Orbiting Carbon Observatory (OCO) 2 and 3 can be used in conjunction with NO_2 imaging satellites to determine CO_2:NO_x ratios and convert the estimated NO_x emissions to CO_2 (Hakkarainen et al., 2021; Reuter et al., 2019). In this way, it is possible to take advantage of the numerous NO_2 imaging satellites with their high temporal resolution to quantify CO_2 emissions globally.

7 Conclusion

The current study aimed to derive a more realistic conversion of NO_2 to NO_x in the plumes of large CO_2 and NO_x sources. In addition, methods for estimating the effective wind speed of the plumes were investigated and a correction to account for coarsely resolved AMFs was implemented. This study built on and expanded the cross-sectional flux method in the Python package *ddeq* and is the first study to systematically apply it to real satellite data.

The results show that with the new findings, annual NO_x emissions can be reliably estimated with TROPOMI: the biases were reduced from between -50 and -60% to only -12 to -23% with of uncertainties of 4 to 19%. These more accurate NO_x emission estimates can be converted to CO_2 emissions using $CO_2:NO_x$ ratios, allowing the use of NO_2 imaging satellites such as GEMS, TEMPO, Sentinel-4, and -5 to estimate CO_2 emission with high temporal resolution until the launch of CO2M in 2025. Furthermore, the geostationary satellites will allow to resolve the diurnal cycle of emissions and could help to reduce the seasonal bias in the number of successful emission estimates due to cloud cover.

Despite the promising results of this study, several knowledge gaps were identified. For example, comprehensive and systematic studies are needed on how to derive the NO_2-to-NO_x conversion factor based on prevailing conditions such as solar radiation, temperature, and background concentrations of reactive trace gases. Thorough research needs to be conducted to determine how wind speeds should be vertically averaged and how well such averaging reflects the effective wind speed of the plume. Further work is also needed on the spatial resolution of a priori NO_2 profiles for the calculation of AMFs to prevent systematic underestimation of NO_2 columns in plumes.

Besides these knowledge gaps, the limitations of estimating CO_2 emissions from satellite-derived NO_x measurements are the uncertainties in converting NO_x to CO_2, as bottom-up reported $CO_2:NO_x$ ratios are uncertain and source specific. On top of that, there are methodological limitations, such as cloud cover, which can severely limit the accuracy of annual emission estimates. In addition, the cross-sectional flux method does not work in the case of overlapping plumes, stagnant wind, and deviations from steady-state conditions.

On the bottom line, this study is a pivotal step towards global, uniform, high-resolution, and near real time estimation of NO_x and CO_2 emissions with the use of satellites. Such independent monitoring and verification can ensure that all countries comply with the Paris Agreement and reduce their CO_2 emissions to tackle anthropogenic climate change.

References

Agustí-Panareda, A., Barré, J., Massart, S., Inness, A., Aben, I., Ades, M., Baier, B.C., Balsamo, G., Borsdorff, T., Bousserez, N., Boussetta, S., Buchwitz, M., Cantarello, L., Crevoisier, C., Engelen, R., Eskes, H., Flemming, J., Garrigues, S., Hasekamp, O., Huijnen, V., Jones, L., Kipling, Z., Langerock, B., Mcnorton, J., Meilhac, N., Noël, S., Parrington, M., Peuch, V.H., Ramonet, M., Razinger, M., Reuter, M., Ribas, R., Suttie, M., Sweeney, C., Tarniewicz, J., Wu, L., 2023. Technical note: The CAMS greenhouse gas reanalysis from 2003 to 2020. Atmos Chem Phys 23, 3829–3859. https://doi.org/10.5194/acp-23-3829-2023

Beirle, S., Boersma, K.F., Platt, U., Lawrence, M.G., Wagner, T., 2011. Megacity emissions and lifetimes of nitrogen oxides probed from space. Science 333, 1737–1739. https://doi.org/10.1126/science.1207824

Beirle, S., Borger, C., Dörner, S., Eskes, H., Kumar, V., de Laat, A., Wagner, T., 2021. Catalog of NO_x emissions from point sources as derived from the divergence of the NO_2 flux for TROPOMI. Earth Syst. Sci. Data 13, 2995–3012. https://doi.org/10.5194/essd-13-2995-2021

Beirle, S., Borger, C., Dörner, S., Li, A., Hu, Z., Liu, F., Wang, Y., Wagner, T., 2019. Pinpointing nitrogen oxide emissions from space. Sci Adv 5. https://doi.org/10.1126/sciadv.aax9800

Berezin, E. V, Konovalov, I.B., Ciais, P., Richter, A., Tao, S., Janssens-Maenhout, G., Beekmann, M., Schulze, E.-D., 2013. Multiannual changes of CO_2 emissions in China: indirect estimates derived from satellite measurements of tropospheric NO_2 columns. Atmos. Chem. Phys. 13, 9415–9438. https://doi.org/10.5194/acp-13-9415-2013

Bovensmann, H., Buchwitz, M., Burrows, J.P., Reuter, M., Krings, T., Gerilowski, K., Schneising, O., Heymann, J., Tretner, A., Erzinger, J., 2010. A remote sensing technique for global monitoring of power plant CO_2 emissions from space and related applications. Atmos. Meas. Tech. 3, 781–811. https://doi.org/10.5194/amt-3-781-2010

Brunner, D., Kuhlmann, G., Marshall, J., Clément, V., Fuhrer, O., Broquet, G., Löscher, A., Meijer, Y., 2019. Accounting for the vertical distribution of emissions in atmospheric CO_2 simulations. Atmos. Chem. Phys. 19, 4541–4559. https://doi.org/10.5194/acp-19-4541-2019

CoCO2, 2023. CoCO2: Prototype system for a Copernicus CO_2 service [WWW Document]. URL https://coco2-project.eu/ (accessed 6.2.23).

Copernicus Climate Change Service, Climate Data Store, 2023. ERA5 hourly data on single levels from 1940 to present. https://doi.org/10.24381/cds.adbb2d47

Copernicus Sentinel-5P, 2021. TROPOMI Level 2 Nitrogen Dioxide total column products. Version 02. European Space Agency. https://doi.org/https://doi.org/10.5270/S5P-9bnp8q8

Crippa, M., Guizzardi, D., Banja, M., Solazzo, E., Muntean, M., Schaaf, E., Pagani F., Monforti-Ferrario, F., Olivier, J.G.J., Quadrelli, R., Risquez Martin, A., Taghavi-Moharamli, P., Grassi, G., Rossi, S., Oom, D., Branco, A., San-Miguel, J., Vignati, E., 2022. CO_2 emissions of all world countries: JRC/IEA/PBL 2022 report. Publications Office of the European Union, Luxembourg. https://doi.org/10.2760/07904

Douros, J., Eskes, H., van Geffen, J., Boersma, K.F., Compernolle, S., Pinardi, G., Blechschmidt, A.-M., Peuch, V.-H., Colette, A., Veefkind, P., 2023. Comparing Sentinel-5P TROPOMI NO_2 column observations with the CAMS regional air quality ensemble. Geosci. Model Dev. 16, 509–534. https://doi.org/10.5194/gmd-16-509-2023

EoPortal, 2023. TEMPO (Tropospheric Emissions: Monitoring of Pollution) [WWW Document]. URL https://www.eoportal.org/satellite-missions/tempo (accessed 7.20.23).

EoPortal, 2021. CO2M (Carbon Dioxide Monitoring) Mission [WWW Document]. URL https://www.eoportal.org/satellite-missions/co2m (accessed 2.21.23).

EoPortal, 2014. Copernicus: Sentinel-4 [WWW Document]. URL https://www.eoportal.org/satellite-missions/copernicus-sentinel-4 (accessed 7.17.23).

EoPortal, 2013. Copernicus: Sentinel-5 [WWW Document]. URL https://www.eoportal.org/satellite-missions/copernicus-sentinel-5 (accessed 7.17.23).

ESA, 2022. Sentinel Online: Sentinel-5P [WWW Document]. URL https://sentinel.esa.int/web/sentinel/missions/sentinel-5p (accessed 3.15.23).

ESA Earth and Mission Science Division, 2020. ESA Copernicus CO_2 Monitoring Mission Requirements Document.

Eskes, H., van Geffen, J., 2021. Product user manual for the TM5 NO_2, SO_2 and HCHO profile auxiliary support product.

Eskes, H., Van Geffen, J., Boersma, F., Eichmann, K.-U., Apituley, A., Pedergnana, M., Sneep, M., Veefkind, J.P., Loyola, D., 2022. Sentinel-5 precursor/TROPOMI Level 2 Product User Manual Nitrogendioxide.

Eskes, H.J., Boersma, K.F., 2003. Averaging kernels for DOAS total-column satellite retrievals. Atmos. Chem. Phys. 3, 1285–1291. https://doi.org/10.5194/acp-3-1285-2003

Eskes, H.J., Eichmann, K.-U., 2023. S5P Mission Performance Centre Nitrogen Dioxide [L2__NO2___] Readme.

European Parliament, Council of the European Union, 2006. REGULATION (EC) No 166/2006: Establishment of a European Pollutant Release and Transfer Register and amending Council Directives 91/689/EEC and 96/61, Official Journal of the European Union. European Parliament and Council.

Flemming, J., Huijnen, V., Arteta, J., Bechtold, P., Beljaars, A., Blechschmidt, A.M., Diamantakis, M., Engelen, R.J., Gaudel, A., Inness, A., Jones, L., Josse, B., Katragkou, E., Marecal, V., Peuch, V.H., Richter, A., Schultz, M.G., Stein, O., Tsikerdekis, A., 2015. Tropospheric chemistry in the integrated forecasting system of ECMWF. Geosci Model Dev 8, 975–1003. https://doi.org/10.5194/gmd-8-975-2015

Goldberg, D.L., Lu, Z., Oda, T., Lamsal, L.N., Liu, F., Griffin, D., McLinden, C.A., Krotkov, N.A., Duncan, B.N., Streets, D.G., 2019a. Exploiting OMI NO_2 satellite observations to infer fossil-fuel CO_2 emissions from U.S. megacities. Science of The Total Environment 695, 133805. https://doi.org/https://doi.org/10.1016/j.scitotenv.2019.133805

Goldberg, D.L., Lu, Z., Streets, D.G., De Foy, B., Griffin, D., Mclinden, C.A., Lamsal, L.N., Krotkov, N.A., Eskes, H., 2019b. Enhanced Capabilities of TROPOMI NO_2: Estimating NO_x from North American Cities and Power Plants. Environ Sci Technol 53, 12594–12601. https://doi.org/10.1021/acs.est.9b04488

Griffin, D., Zhao, X., McLinden, C.A., Boersma, F., Bourassa, A., Dammers, E., Degenstein, D., Eskes, H., Fehr, L., Fioletov, V., Hayden, K., Kharol, S.K., Li, S.M., Makar, P., Martin, R. V., Mihele, C., Mittermeier, R.L., Krotkov, N., Sneep, M., Lamsal, L.N., Linden, M. ter, Geffen, J. van, Veefkind, P., Wolde, M., 2019. High-Resolution Mapping of Nitrogen Dioxide With TROPOMI: First Results and Validation Over the Canadian Oil Sands. Geophys Res Lett 46, 1049–1060. https://doi.org/10.1029/2018GL081095

Gualtieri, G., 2022. Analysing the uncertainties of reanalysis data used for wind resource assessment: A critical review. Renewable and Sustainable Energy Reviews 167, 112741. https://doi.org/https://doi.org/10.1016/j.rser.2022.112741

Guan, D., Liu, Z., Geng, Y., Lindner, S., Hubacek, K., 2012. The gigatonne gap in China's carbon dioxide inventories. Nat Clim Chang 2, 672–675. https://doi.org/10.1038/nclimate1560

Guevara, M., Enciso, S., Tena, C., Jorba, O., Dellaert, S., Denier van der Gon, H., Pérez García-Pando, C., 2023a. CoCO2 global emission point source database. https://doi.org/10.24380/mxjo-nram

Guevara, M., Enciso, S., Tena, C., Jorba, O., Dellaert, S., Denier van der Gon, H., Pérez García-Pando, C., 2023b. A global catalogue of CO_2 emissions and co-emitted species from power plants at a very high spatial and temporal resolution [Preprint]. Earth Syst Sci Data 1–41. https://doi.org/10.5194/essd-2023-95

Gurney, K.R., Huang, J., Coltin, K., 2016. Bias present in US federal agency power plant CO_2 emissions data and implications for the US clean power plan. Environmental Research Letters 11, 064005. https://doi.org/10.1088/1748-9326/11/6/064005

Hakkarainen, J., Szeląg, M.E., Ialongo, I., Retscher, C., Oda, T., Crisp, D., 2021. Analyzing nitrogen oxides to carbon dioxide emission ratios from space: A case study of Matimba Power Station in South Africa. Atmos Environ X 10, 100110. https://doi.org/https://doi.org/10.1016/j.aeaoa.2021.100110

Hakkarainen, J., Tamminen, J., Nurmela, J., Lindqvist, H., Santaren, D., Broquet, G., Chevallier, F., Koene, E., Kuhlmann, G., Brunner, D., 2023. D4.4 Benchmarking of plume detection and quantification methods.

Hersbach, H., Bell, B., Berrisford, P., Biavati, G., Horányi, A., Muñoz Sabater, J., Nicolas, J., Peubey, C., Radu, R., Rozum, I., Schepers, D., Simmons, A., Soci, C., Dee, D., Thépaut, J.-N., 2023. ERA5 hourly data on single levels from 1940 to present. https://doi.org/10.24381/cds.adbb2d47

Hill, T., Nassar, R., 2019. Pixel Size and Revisit Rate Requirements for Monitoring Power Plant CO2 Emissions from Space. Remote Sens (Basel) 11. https://doi.org/10.3390/rs11131608

Honnert, R., Masson, V., Lac, C., Nagel, T., 2021. A Theoretical Analysis of Mixing Length for Atmospheric Models From Micro to Large Scales. Front Earth Sci (Lausanne) 8, 582056. https://doi.org/10.3389/feart.2020.582056

Huijnen, V., Flemming, J., Chabrillat, S., Errera, Q., Christophe, Y., Blechschmidt, A.-M., Richter, A., Eskes, H., 2016. C-IFS-CB05-BASCOE: stratospheric chemistry in the Integrated Forecasting System of ECMWF. Geosci. Model Dev. 9, 3071–3091. https://doi.org/10.5194/gmd-9-3071-2016

Huijnen, V., Le Sager, P., Köhler, M.O., Carver, G., Rémy, S., Flemming, J., Chabrillat, S., Errera, Q., Van Noije, T., 2022. OpenIFS/AC: atmospheric chemistry and aerosol in OpenIFS 43r3. Geosci Model Dev 15, 6221–6241. https://doi.org/10.5194/gmd-15-6221-2022

IPCC, 2006. 2006 IPCC guidelines for national greenhouse gas inventories. Institute for Global Environmental Strategies, Japan.

Jaffe, D., 2003. Nitrogen Cycle, Atmospheric, in: Meyers, R.A.B.T.-E. of P.S. and T. (Third E. (Ed.), Encyclopedia of Physical Science and Technology. Academic Press, New York, pp. 431–440. https://doi.org/https://doi.org/10.1016/B0-12-227410-5/00922-4

Kimbrough, S., Chris Owen, R., Snyder, M., Richmond-Bryant, J., 2017. NO to NO_2 conversion rate analysis and implications for dispersion model chemistry methods using Las Vegas, Nevada near-road field measurements. Atmos Environ 165, 23–34. https://doi.org/10.1016/j.atmosenv.2017.06.027

Koene, E., Brunner, D., 2023. D4.2 Assessment of Plume Model Performance.

Koene, E., Brunner, D., Kuhlmann, G., Hakkarainen, J., Dumont Le Brazidec, J., Broquet, G., 2021. D4.3 Documentation of plume detection and quantification methods.

Krol, M., Van Stratum, B., 2021. D4.1 Definition of simulation cases and model system for building a library of plumes.

Kuhlmann, G., Amarós, L., Gregoire, Broquet Dominik, Brunner Frédéric, C., Hakkarainen, J., Koene, E., Meier, S., Nurmela, J., Santaren, D., Tamminen, J., 2023. Data-driven emission quantification: Gitlab repository [WWW Document]. URL https://gitlab.com/empa503/remote-sensing/ddeq (accessed 3.17.23).

Kuhlmann, G., Broquet, G., Marshall, J., Clément, V., Löscher, A., Meijer, Y., Brunner, D., 2019. Detectability of CO_2 emission plumes of cities and power plants with the Copernicus Anthropogenic CO_2 Monitoring (CO2M) mission. Atmos. Meas. Tech. 12, 6695–6719. https://doi.org/10.5194/amt-12-6695-2019

Kuhlmann, G., Brunner, D., Broquet, G., Meijer, Y., 2020. Quantifying CO_2 emissions of a city with the Copernicus Anthropogenic CO_2 Monitoring satellite mission. Atmos. Meas. Tech. 13, 6733–6754. https://doi.org/10.5194/amt-13-6733-2020

Kuhlmann, G., Chan, K.L., Donner, S., Zhu, Y., Schwaerzel, M., Dörner, S., Chen, J., Hueni, A., Nguyen, D.H., Damm, A., Schütt, A., Dietrich, F., Brunner, D., Liu, C., Buchmann, B., Wagner, T., Wenig, M., 2022. Mapping the spatial distribution of NO_2 with in situ and remote sensing instruments during the Munich NO_2 imaging campaign. Atmos. Meas. Tech. 15, 1609–1629. https://doi.org/10.5194/amt-15-1609-2022

Kuhlmann, G., Clément, V., Marshall, J., Fuhrer, O., Broquet, G., Schnadt-Poberaj, C., Löscher, A., Meijer, Y., Brunner, D., 2018. SMARTCARB – Use of Satellite Measurements of Auxiliary Reactive Trace Gases for Fossil Fuel Carbon Dioxide Emission Estimation, Final report of ESA study contract n°4000119599/16/NL/FF/mg, project led by Empa (Switzerland).

Kuhlmann, G., Henne, S., Meijer, Y., Brunner, D., 2021. Quantifying CO_2 Emissions of Power Plants With CO_2 and NO_2 Imaging Satellites. Frontiers in Remote Sensing 2, 1–18. https://doi.org/10.3389/frsen.2021.689838

Liu, F., Duncan, B.N., Krotkov, N.A., Lamsal, L.N., Beirle, S., Griffin, D., McLinden, C.A., Goldberg, D.L., Lu, Z., 2020. A methodology to constrain carbon dioxide emissions from coal-fired power plants using satellite observations of co-emitted nitrogen dioxide. Atmos. Chem. Phys. 20, 99–116. https://doi.org/10.5194/acp-20-99-2020

Lohmann, U., Lüönd, F., Mahrt, F., 2016. An introduction to clouds: From the microscale to climate. Cambridge University Press.

Lorente, A., Boersma, K.F., Eskes, H.J., Veefkind, J.P., van Geffen, J.H.G.M., de Zeeuw, M.B., Denier van der Gon, H.A.C., Beirle, S., Krol, M.C., 2019. Quantification of nitrogen oxides emissions from build-up of pollution over Paris with TROPOMI. Sci Rep 9, 1–10. https://doi.org/10.1038/s41598-019-56428-5

Nassar, R., Hill, T.G., McLinden, C.A., Wunch, D., Jones, D.B.A., Crisp, D., 2017. Quantifying CO_2 Emissions From Individual Power Plants From Space. Geophys Res Lett 44, 10,10-45,53. https://doi.org/https://doi.org/10.1002/2017GL074702

Nassar, R., Moeini, O., Mastrogiacomo, J.-P., O'Dell, C.W., Nelson, R.R., Kiel, M., Chatterjee, A., Eldering, A., Crisp, D., 2022. Tracking CO2 emission reductions from space: A case study at Europe's largest fossil fuel power plant. Frontiers in Remote Sensing. https://doi.org/https://doi.org/10.3389/frsen.2022.1028240

NLMK Group, 2021. Annual Report 2021 [WWW Document]. URL https://nlmk.com/en/ir/results/annual-reports/ (accessed 2.6.23).

Pietrzyk, B., Wojtas, J., Bielecki, Z., Mikolajczyk, J., Nowakowski, M., 2010. Application of an optical parametric generator to cavity enhanced experiment. Photonics Applications in Astronomy, Communications, Industry, and High-Energy Physics Experiments 7745. https://doi.org/10.1117/12.872228

Pinty, B., Dowell, M., Zunker, H., Andersson, E., Balsamo, G., Bézy, J., Brunhes, T., Bösch, H., Bojkov, B., Brunner, D., Buchwitz, M., Crisp, D., Scholze, M., Sierk, B., Tamminen, J., Veefkind, P., 2020. Toward an Operational Anthropogenic CO_2 Emissions Monitoring and Verification Support Capacity. Bull Am Meteorol Soc 1439–1451.

Pinty, B., Janssens-Maenhout, G., Dowell, M., Zunker, H., Brunhes, T., Ciais, P., Dee, D., Denier Van Der Gon, H., Dolman, H., Drinkwater, M., Engelen, R., Heimann, M., Holmlund, K., Husband, R., Kentarchos, A., Meijer, Y., Palmer, P., Scholze, M., 2017. An operational anthropogenic CO2 emissions monitoring & verification system: baseline requirements, model components and functional architecture. Publications Office of the European Union, Luxembourg. https://doi.org/doi/10.2760/08644

Platt, U., Stutz, J., 2008. Differential Optical Absorption Spectroscopy: Principles and Applications, 1st ed. Springer Berlin, Heidelberg. https://doi.org/https://doi.org/10.1007/978-3-540-75776-4

Potts, D.A., Timmis, R., Ferranti, E.J.S., Vande Hey, J.D., 2023. Identifying and accounting for the Coriolis effect in satellite NO_2 observations and emission estimates. Atmos. Chem. Phys. 23, 4577–4593. https://doi.org/10.5194/acp-23-4577-2023

Pronobis, M., 2020. Reduction of nitrogen oxide emissions, in: Environmentally Oriented Modernization of Power Boilers. Elsevier, pp. 79–133. https://doi.org/10.1016/b978-0-12-819921-3.00004-2

Reuter, M., Buchwitz, M., Hilboll, A., Richter, A., Schneising, O., Hilker, M., Heymann, J., Bovensmann, H., Burrows, J.P., 2014. Decreasing emissions of NO_x relative to CO_2 in East Asia inferred from satellite observations. Nat Geosci 7, 792–795. https://doi.org/10.1038/ngeo2257

Reuter, M., Buchwitz, M., Schneising, O., Krautwurst, S., O'Dell, C.W., Richter, A., Bovensmann, H., Burrows, J.P., 2019. Towards monitoring localized CO_2 emissions from space: Co-located regional CO_2 and NO_2 enhancements observed by the OCO-2 and S5P satellites. Atmos Chem Phys 19, 9371–9383. https://doi.org/10.5194/acp-19-9371-2019

Seinfeld, J.H., Pandis, S.N., 2006. Atmospheric chemistry and physics: From air pollution to climate change, 2nd ed. Wiley, New York.

Skalska, K., Miller, J.S., Ledakowicz, S., 2010. Trends in NOx abatement: A review. Science of the Total Environment 408, 3976–3989. https://doi.org/10.1016/j.scitotenv.2010.06.001

UNECE, 2015. Guidelines for Reporting Emissions and Projections Data under the Convention on Long-range Transboundary Air Pollution, United Nations Economic Commission for Europe. New York and Geneva.

UNFCCC, 2015. Paris Agreement [WWW Document]. URL http://unfccc.int/resource/docs/2015/cop21/eng/l09r01.pdf (accessed 2.21.23).

United Nations, 2015. United Nations Treaty Collection [WWW Document]. URL https://treaties.un.org/doc/Publication/MTDSG/Volume II/Chapter XXVII/XXVII-7-d.en.pdf (accessed 2.21.23).

van Geffen, J., Eskes, H., Compernolle, S., Pinardi, G., Verhoelst, T., Lambert, J.-C., Sneep, M., Linden, M. Ter, Ludewig, A., Boersma, K.F., Veefkind, J.P., 2022. Sentinel-5P TROPOMI NO2 retrieval: impact of version v2.2 improvements and comparisons with OMI and ground-based data. Atmos Meas Tech 15, 2037–2060. https://doi.org/10.5194/amt-15-2037-2022

van Geffen, J., Eskes, H.J., Boersma, K.F., Veefkind, J.P., 2019. TROPOMI ATBD of the total and tropospheric NO2 data products, Tech. Rep. S5P-KNMI-L2-0005-RP.

van Heerwaarden, C.C., van Stratum, B.J.H., Heus, T., Gibbs, J.A., Fedorovich, E., Mellado, J.P., 2017. MicroHH 1.0: a computational fluid dynamics code for direct numerical simulation and large-eddy simulation of atmospheric boundary layer flows. Geosci. Model Dev. 10, 3145–3165. https://doi.org/10.5194/gmd-10-3145-2017

Varon, D.J., Jacob, D.J., McKeever, J., Jervis, D., Durak, B.O.A., Xia, Y., Huang, Y., 2018. Quantifying methane point sources from fine-scale satellite observations of atmospheric methane plumes. Atmos. Meas. Tech. 11, 5673–5686. https://doi.org/10.5194/amt-11-5673-2018

Veefkind, J.P., Aben, I., McMullan, K., Förster, H., de Vries, J., Otter, G., Claas, J., Eskes, H.J., de Haan, J.F., Kleipool, Q., van Weele, M., Hasekamp, O., Hoogeveen, R., Landgraf, J., Snel, R., Tol, P., Ingmann, P., Voors, R., Kruizinga, B., Vink, R., Visser, H., Levelt, P.F., 2012. TROPOMI on the ESA Sentinel-5 Precursor: A GMES mission for global observations of the atmospheric composition for climate, air quality and ozone layer applications. Remote Sens Environ 120, 70–83. https://doi.org/https://doi.org/10.1016/j.rse.2011.09.027

Verhoelst, T., Compernolle, S., Pinardi, G., Lambert, J.-C., Eskes, H.J., Eichmann, K.-U., Fjæraa, A.M., Granville, J., Niemeijer, S., Cede, A., Tiefengraber, M., Hendrick, F., Pazmiño, A., Bais, A., Bazureau, A., Boersma, K.F., Bognar, K., Dehn, A., Donner, S., Elokhov, A., Gebetsberger, M., Goutail, F., Grutter de la Mora, M., Gruzdev, A., Gratsea, M., Hansen, G.H., Irie, H., Jepsen, N., Kanaya, Y., Karagkiozidis, D., Kivi, R., Kreher, K., Levelt, P.F., Liu, C., Müller, M., Navarro Comas, M., Piters, A.J.M., Pommereau, J.-P., Portafaix, T., Prados-Roman, C., Puentedura, O., Querel, R., Remmers, J., Richter, A., Rimmer, J., Rivera Cárdenas, C., Saavedra de Miguel, L., Sinyakov, V.P., Stremme, W., Strong, K., Van Roozendael, M., Veefkind, J.P., Wagner, T., Wittrock, F., Yela González, M., Zehner, C., 2021. Ground-based validation of the Copernicus Sentinel-5P TROPOMI NO_2 measurements with the NDACC ZSL-DOAS, MAX-DOAS and Pandonia global networks. Atmos. Meas. Tech. 14, 481–510. https://doi.org/10.5194/amt-14-481-2021

Wallace, J.M., Hobbs, P. V, 2006. Atmospheric Science: An Introductory Survey Academic Press, 2nd ed, New York. Academic Press. https://doi.org/https://doi.org/10.1016/C2009-0-00034-8

Williams, J.E., Boersma, K.F., Le Sager, P., Verstraeten, W.W., 2017. The high-resolution version of TM5-MP for optimized satellite retrievals: description and validation. Geosci. Model Dev. 10, 721–750. https://doi.org/10.5194/gmd-10-721-2017

Zhao, Y., Nielsen, C.P., Lei, Y., McElroy, M.B., Hao, J., 2011. Quantifying the uncertainties of a bottom-up emission inventory of anthropogenic atmospheric pollutants in China. Atmos. Chem. Phys. 11, 2295–2308. https://doi.org/10.5194/acp-11-2295-2011
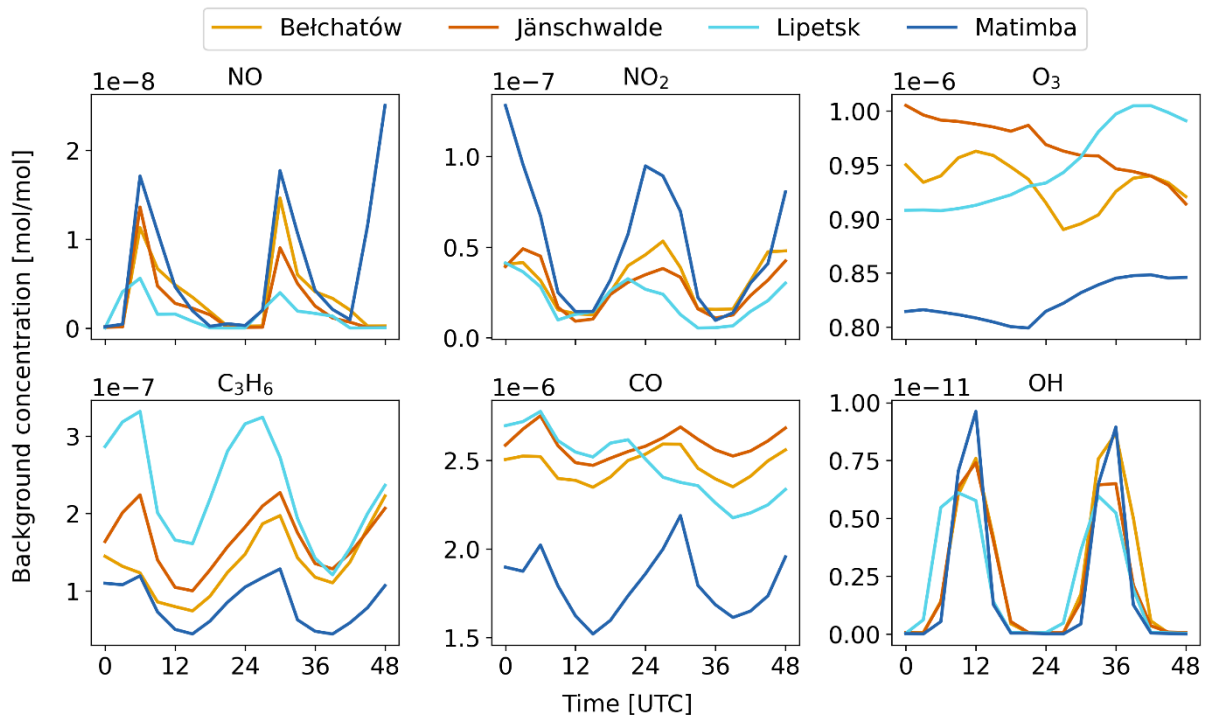
A. Appendix

Figure A.1: Vertically integrated background concentrations of reactive trace gases of the MicroHH simulations for Bełchatów, Jänschwalde, Lipetsk, and Matimba.
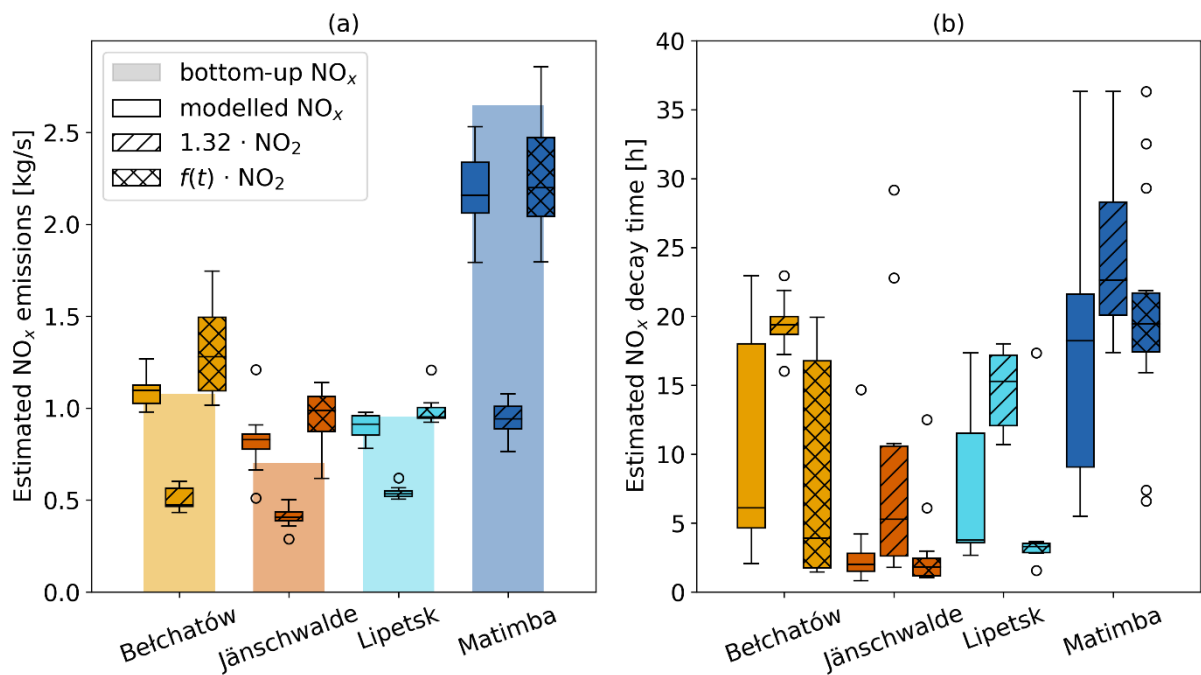
Figure A.2: (a) Comparison of estimated NO_x emissions against the bottom-up reported and (b) estimated NO_x decay times using the old and new algorithms as well as the modelled NO_x fields. For the wind speed, the backward integrated wind was used.
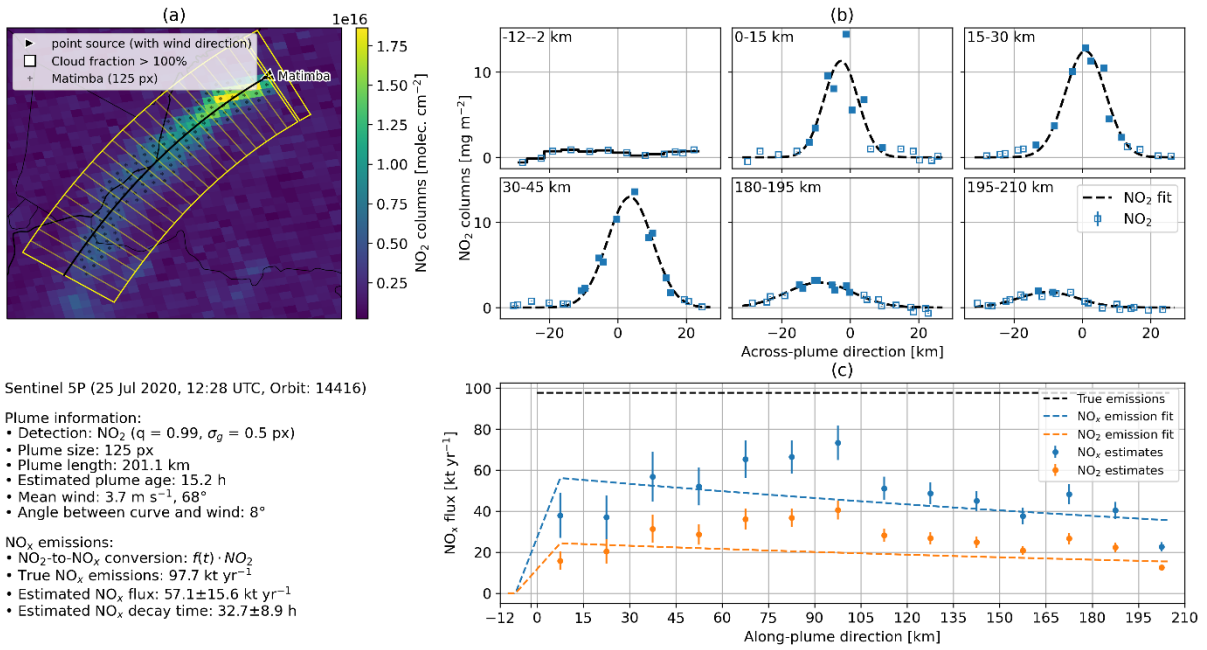
Figure A.3: Estimated NO_x emissions for the TROPOMI image on the 25th of July 2020 using default NO_2 profiles.
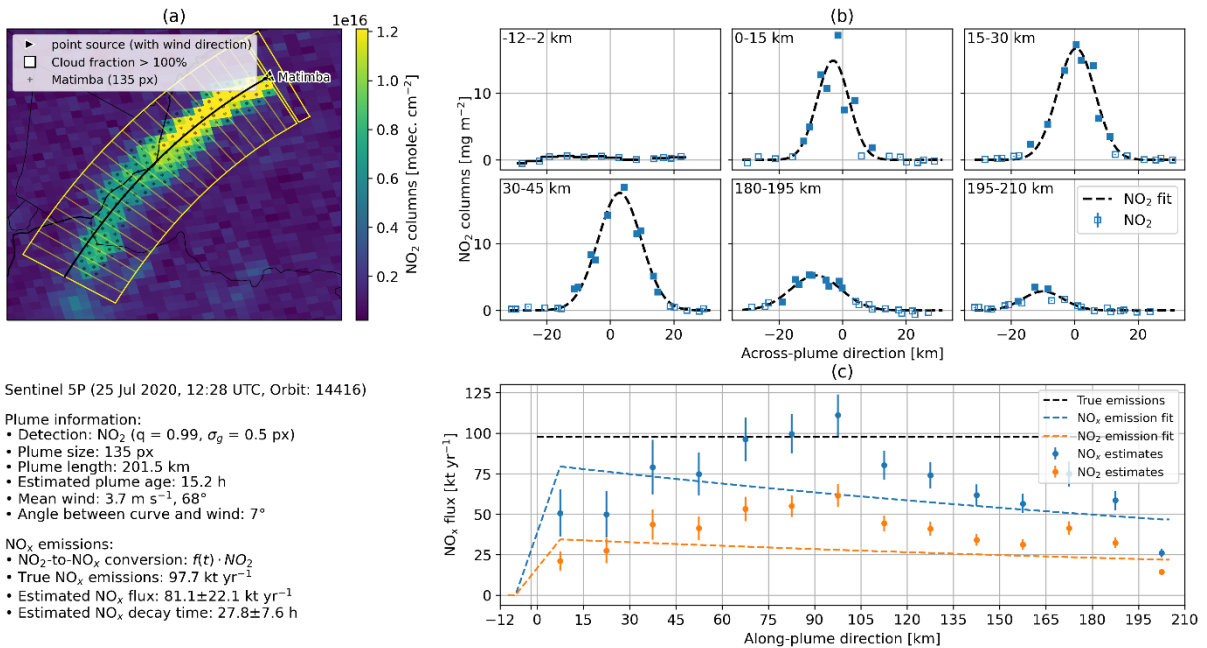

Figure A.4: Estimated NO_x emissions for the TROPOMI image on the 25th of July 2020 using updated NO_2 profiles within ($5 \cdot 10^{-9}$ mol/mol) and outside ($2 \cdot 10^{-10}$ mol/mol) of the plume.
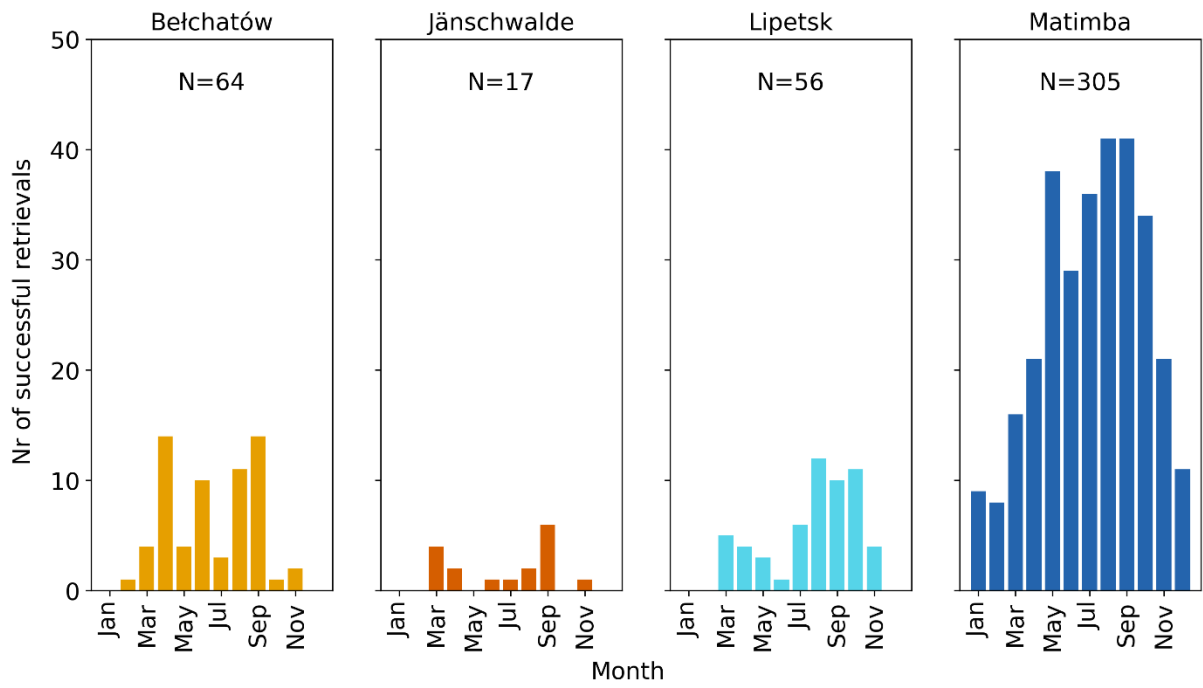
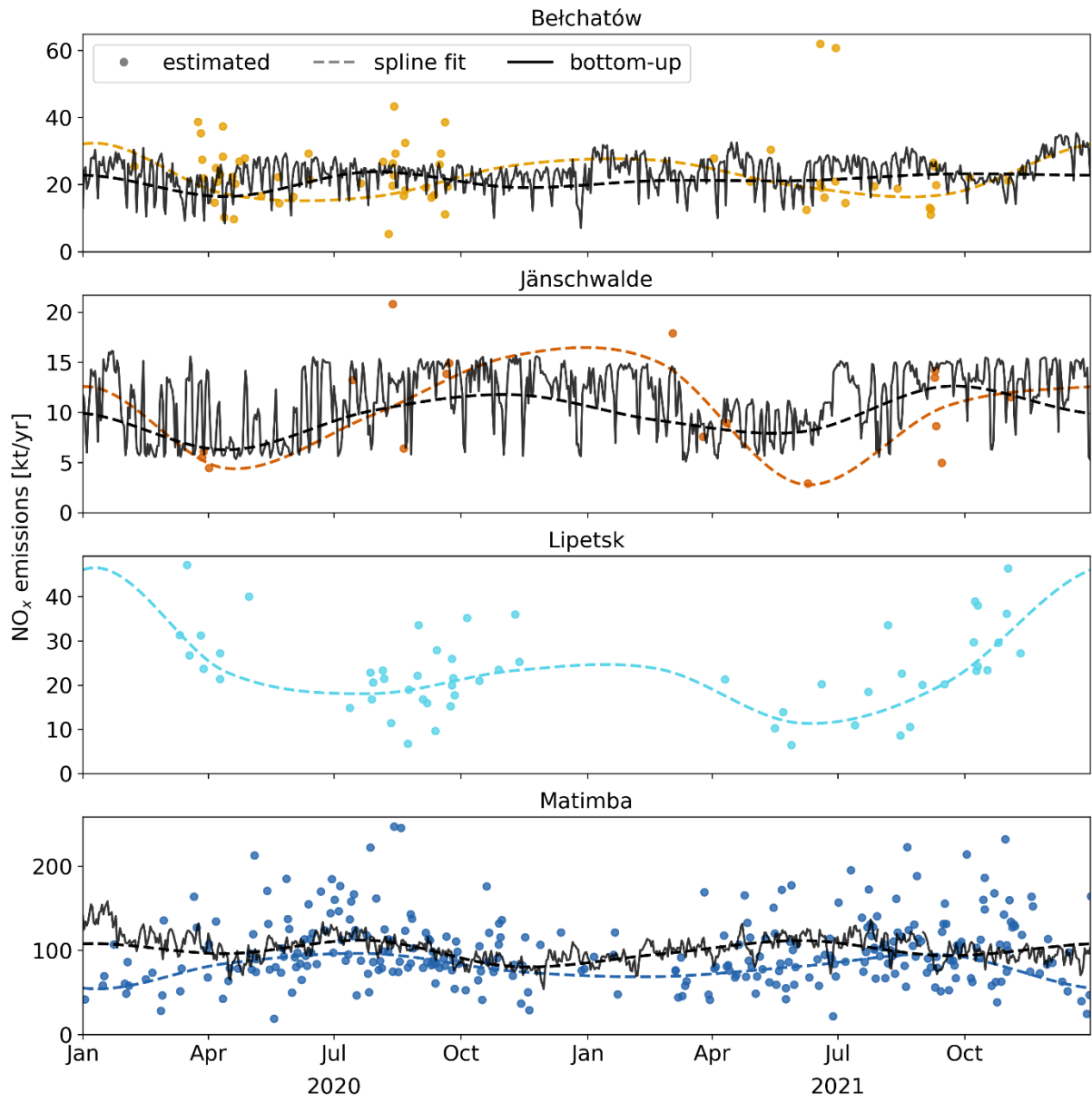Figure A.5: Number of successful NO$_x$ emission estimates per month using TROPOMI for 2020 and 2021.

Figure A.6: Time series of NO$_x$ emission estimates using TROPOMI and bottom-up reported emissions for the years 2020 and 2021. To each time series, a cubic Hermite spline with periodic boundary conditions was fitted.

Declaration of Authorship

Personal declaration: I hereby declare that the submitted Thesis is the result of my own, independent work. All external sources are explicitly acknowledged in the Thesis.

Signature: _____S. Meier_____

Date: _____9th August 2023_____